

Progress in Magnus Type Wind Turbine Theories

AHMAD SEDAGHAT

ABSTRACT

A large number of researches have been conducted on increasing lift to drag ratio of aerofoils used in the commercial type horizontal axis wind turbines. For the most efficient aerofoils in practical situations, the maximum lift to drag ratio is less than 200. One of the attracting concepts to produce high lift is by using the Magnus type devices. Traditionally, the Magnus effect is misinterpreted as generation of high lift force from spinning cylinders, spheres, or disks. However, the Magnus lift can be produced from circulating any aerodynamic shape. With progressing innovative Magnus type wind turbine generators, it is essential to analysis such devices as correctly as possible. First, the importance of research carried out on the flow around rotating circular cylinders is highlighted and reviewed here. Then, the theoretical methods used in modelling aerodynamics of the commercial aerofoil type wind turbines are extended and applied on the Magnus types. The potential flow analysis is developed around the Magnus type blades and the blade element momentum (BEM) theory formulation is extended for the Magnus type wind turbines. From the BEM analysis, a cubic function based on the angular induction factor is obtained which its coefficients are dependent on the axial induction factor, the local speed ratio, and the drag to lift ratio. The resulted power coefficient of the Magnus type wind turbine seems strongly dependent on the drag to lift ratio. Next by examining drag to lift ratio of spinning cylinders as reported by a number of computational or experimental works, it is realized that the generation of high lift to drag ratio from spinning cylinders is a very difficult job because the drag force is simultaneously increases by increasing lift. Second, the generation of high lift to drag ratio

Department of Mechanical Engineering, Isfahan University of Technology, Isfahan, 84156-83111, I. R. of Iran

*Corresponding author: E-mail: sedaghat@cc.iut.ac.ir; Web address: <http://sedaghat.iut.ac.ir/>

is sought by studying circulating aerofoil surfaces rather than spinning cylinders. To see that the Magnus effect can also be produced by the circulating aerofoil surfaces, the symmetrical NACA0015 aerofoil with treadmill like motion of its surface is computationally investigated. The governing RANS equations of compressible fluid flow motion are solved using a class of implicit, time marching, high-resolution, second order accurate, symmetric and upwind TVD schemes around the aerofoil section in a C-type structured algebraic-hyperbolic mesh. The zero-equation Baldwin-Lomax turbulence model was employed at this stage. At zero angle of attack, non-zero values of the lift force reveals that the Magnus force can also be produced by circulating aerofoils. Examining this at different incidence angles and treadmill speeds, it is approved that a favourable increase in lift coefficient simultaneously with decrease in drag coefficient is achieved. Interestingly, an approximately near to zero drag value can be achieved at around the incident angle of 5 degrees with a dimensionless treadmill speed of 3 which produces a lift to drag ratio of 684; although, the accuracy of the present computational results should be improved using more advanced turbulence models. This is still very promising compared with the most efficient aerofoils used in conventional wind turbines. The emerging treadmill concept may be further investigated experimentally to fully discover all its features and merits for application in Magnus type wind turbines and industrial manufacturing processes.

Key words: Wind power, Magnus effect, Horizontal axis wind turbine, Potential flow, CFD, Treadmill motion, Circulating aerofoils, Blade element momentum theory

1. INTRODUCTION

The Magnus effect is referred to generation of lift from spinning cylinders or spheres. The lift force generated by Magnus effect is much larger than streamlined aerofoils. This has motivated a large number of researchers and scientist to use the Magnus lift in aerospace, naval, and wind turbine industries. Perhaps it was Anton Flettner who has patented of using Magnus lift and employed it in his ship Buckau^[1]. In 1924, Flettner has built his ship propelling with two high rise rotating cylinders. The Flettner type rotor was perhaps the first successful device based on Magnus effect; although, his device was not commercialized due to decrease in oil prices at that time. The potential of producing high lift forces then attracted many researchers in aeronautics. Many reported patents were appeared in the areas of naval or aerospace applications based on using Magnus forces. But, very few devices were operated successfully. The renew interest in the Flettner type rotor is becoming again a hot topic in naval engineering due to the increase in fuel costs and environmental crisis such as global warming. Seifert^[1] has extensively reviewed the application of Magnus forces in aeronautics who believes that there are no specific methods available for

designing lifting devices using Magnus effects. This is particularly observed on works reported on Magnus wind turbines.

The aim of this study is to elaborate the numerous experimental and computational findings on lift and drag forces over rotating circular cylinders for development of theories used in the horizontal axis wind turbines to be extended into Magnus type wind turbines. Theories studied here include the development of potential flow around spinning blades, the one-dimensional linear and angular momentum conservation laws, the blade element theory, and the combined blade element momentum theory (BEM). These classical theories are developed and extended for application in aerodynamic modeling of the horizontal axis Magnus type wind turbines. For general aerodynamic geometries with circulating skin, the computational fluid dynamics (CFD) methods may be employed to find lift to drag ratio at prescribed flow and circulating skin conditions. An example of flow conditions over NACA0015 aerofoil with circulating skin is presented here.

1.1. Manufactured or Experimented Magnus Type Wind Turbines

Bychkov^[2] has introduced an experimental approach for which a wind turbine with rotating Magnus cylinders can operate optimally instead of the traditional aerofoil type blades. His studies suggest that the optimal Magnus type wind turbine uses 6 rotating cylinders (see Fig. 1) and operates at high rotational speeds of 8000 rpm. The aspect ratio of 15 is also suggested for

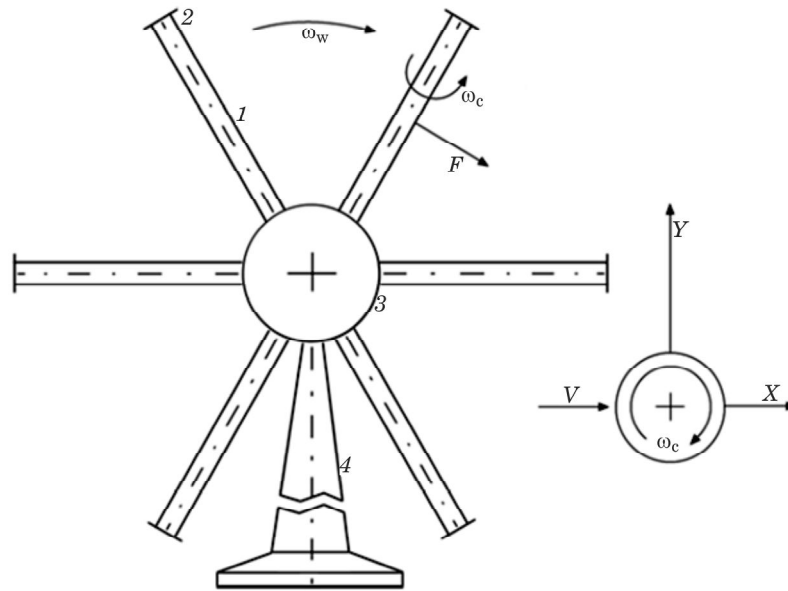


Fig. 1: The Bychkov's optimum horizontal axis Magnus type wind turbine^[2]

optimum cylinders. Bychkov^[2] believes the optimal Magnus wind turbines can compete with the commercial aerofoil type wind turbines at low wind speeds below 8 m/s. The cut-in wind speed of 1–2 m/s is promising outlook for the sites with low wind speeds.

Murakami and co-workers^[3,4] have patented a Magnus type wind turbine with 6 and 5 rotating cylinders in 2007 and 2010, respectively. The cylindrical blades use some spiral ribs in this Magnus type wind turbines. More recently, Mecaro Co^[5] in Japan have manufactured the Murakami's Magnus wind turbines. For the Murakami patented in 2010, the Magnus wind turbine with 5 blades produces 3 kW electrical power at the rated wind speeds of 8 m/s and starts at cut-in wind speeds above 4 m/s. The rotational speed is given to be 1080 rpm; although, no results were given for wind speeds above 8 m/s^[4].

Another small prototyped Chiral blade system was experimentally tested by Giudice and Rosa^[6] for application in hydroelectric microgeneration. They have tested the wind turbine using air flow at low speeds and also analyzed their system using the potential flow solution around two-dimensional rotating cylinders. The theoretical-experimental investigation suggested

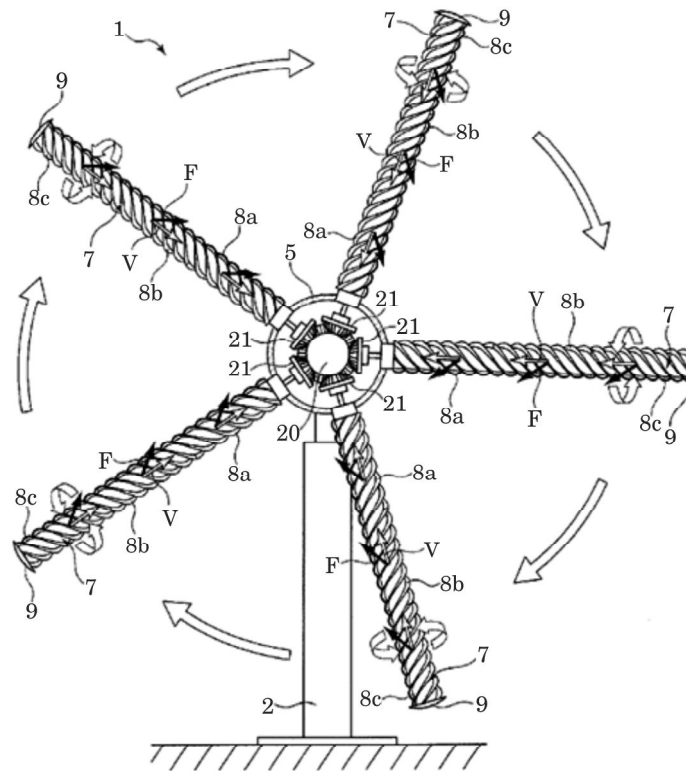


Fig. 2: The Murakami *et al.*^[4] new horizontal axis Magnus type wind turbine

that the micro generator based on both wind and hydro power has great potential particularly for the low head water flows freely available in rivers, tides and offshore currents.

Komatinovic^[7] has extensively investigated several Savonius-type Magnus wind turbines with using both CFD and experiment. The results of 2D simulations suggested the proper Savonius configurations for which Komatinovic has built five most promising prototype blades. The torque and rotational speed of the wind turbines were measured using different sets of 2, 3, 4, and 5 bladed wind turbines in a wind tunnel. Experiments were repeated exclusively at various wind speeds; but, no measurement data were produced for lift and drag forces of the cross section of each blade. The measurements of the cross sectional lift and drag forces are very important to evaluate the power capture of a wind turbine blade. The power captures of all prototype rotor models were reported to be very low; *e.g.* the maximum power coefficient was lower than 0.1.

1.2. Lift, Drag, and Frictional Torque of Spinning Cylinders

The earliest experimental studies on rotating cylinders were probably conducted by Reid^[8] in 1925. He used smooth pinning cylinder in the leading edge of wings. Reid^[8] reported considerable increase in lift force of the wing by employing the rotating cylinders at various rotational speeds up to 3600 rpm at different Reynolds numbers. In 1957, the boundary layer theory over rotating circular cylinders was developed by Glauert^[9]. In 1983, Ingham^[10] reported computational solutions of flows over rotating cylinders at very small Reynolds numbers. The aim of his studies was to assess the viscous effects over rotating cylinders.

Mittal and Bhaskar^[11] have used a dimensionless spin ratio $\acute{\omega}$ which was varied between 0 and 5 to study two-dimensional incompressible flows over a spinning circular cylinder at Reynolds number of 200. The vortex shedding was observed at $\acute{\omega} < 1.91$. At higher spinning rates, flow is steady except within the range of $4.34 < \acute{\omega} < 4.70$ where the flow becomes again unstable. For high rotation rates, very large lift coefficients were observed; however, power consumed to spin the cylinders increases rapidly with spinning rate.

In viscous steady-state flows, vorticity created at a solid surface is convected and diffused. Prandtl believed in existence of an equilibrium state approaches at $\acute{\omega} = 2$. This equilibrium limit prohibits further increase of lift at higher spinning rates. He concluded that the maximum achievable lift value equals to $C_{Lmax} = 4\pi \approx 12.6$. However, Tokumaru and Dimotakis^[12] experimental and numerical observations revealed that there is no such maximum lift limit and the lift can be exceeded this value at higher aspect ratios and higher rotational speeds due to unsteady effects. In high Reynolds flow region of $4 \times 10^4 < Re < 6.6 \times 10^5$, which are within range of practical conditions, the experimental and numerical results of^[12,13] suggested that a

practical range for using Magnus effects is $2 < \dot{\omega} < 4$. This will keep drag coefficient at lowest possible values. Additionally, the linear increase of lift force at different rotating speed of cylinders may be halted due to instabilities, 3D effects, or centrifugal forces across the blade. The developments of instabilities and violations from the maximum lift at high Reynolds numbers was also observed by some computational evidences^[14,15] based on simulation of the Navier-Stokes equations at high spin rates.

Viscous fluid flow around spinning cylinders are usually characterised by the Reynolds number $Re = V_{\infty}D/\nu$ and the spinning ratio $\dot{\omega} = \omega D/2V_{\infty}$ and the desired measured parameters are the magnitude of the lift and drag forces and also friction torque^[1,8,14]. Many of such studies are related to very low Reynolds numbers which is less concerns for practical situations. For relatively high Reynolds numbers as shown in Fig. 3, the variation of lift coefficient (C_L) for a spinning circular cylinder are plotted against drag coefficient (C_D) at the Reynolds number range of ($10^4 \leq Re \leq 10^5$) and the spinning ratio of $0 \leq \dot{\omega} \leq 4$ ^[14]. The experimental results of^[14] for lift and drag coefficients are also correlated with the below fit functions in the equations (1) and (2).

$$C_L = -0.01355 - 0.4065\dot{\omega} + 1.2944\dot{\omega}^2 + 0.2249\dot{\omega}^3 - 0.09632\dot{\omega}^4$$

$$C_D = 1.0631 - 0.9137\dot{\omega} + 0.4694\dot{\omega}^2 \quad (1)$$

The lift and drag polar distribution may also fitted with the following formula:

$$C_D = 0.8954 - 0.1988C_L + 0.04634C_L^2 \quad (2)$$

The above relations (1) to (3) is not seen as a generalized relations for lift and drag of the spinning circular cylinders at the prescribed range of Reynolds numbers; but, it will provides a useful guideline that such formulations based on extensive numerical and experimental may be required for designing and modelling of Magnus wind turbines.

The recent results of the experimental and numerical works of^[14] are compared with the oldest experiments in^[14] and with the above correlated fits (1) and (2) in Fig. 3. As it can be seen from Fig. 3, there is considerable mismatch between the results of^[14] and^[8] and also the numerical results of^[14] under predicted lift values than their experiments^[14]. In overall, the experiments^[8] have predicted much higher lift and lower drag compared with^[14]. Considering the most recent results of^[14], the lift to drag ratio (C_L/C_D) is also plotted against the spinning ratio and is compared with our correlated relations (1) in Fig. 4. As seen in Fig. 4, the lift to drag ratio is possess its maximum peak value near the range of $1.5 \leq \dot{\omega} \leq 2.5$; this range may be considered as the optimum range for design and modelling of Magnus

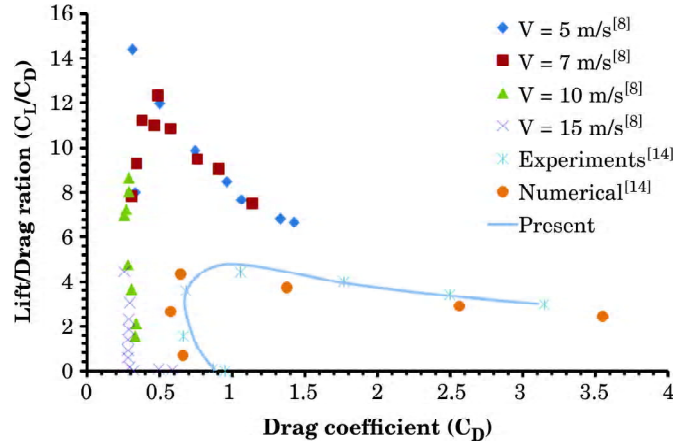


Fig. 3: Lift to drag polar for spinning cylinders at $10^4 \leq Re \leq 10^5$ (Experiments^{[14],[8]}, and numerical of^[14])

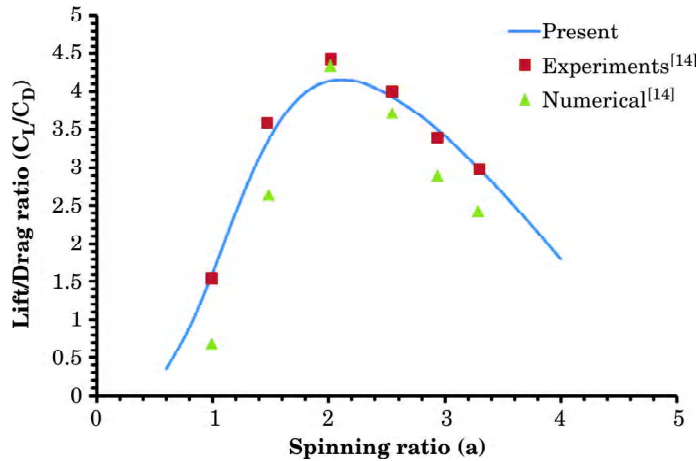


Fig. 4: Lift to drag ratio against cylinder spinning ratio at $10^4 \leq Re \leq 10^5$ (Experiments and numerical results of^[14])

type wind turbine; although, more extensive numerical and experimental works is needed for designing a successful Magnus system.

In order that a Magnus type wind turbine can compete with a traditional aerofoil type wind turbine, the power consumed by the rotating cylinders must be reduced to minimum. The experimental study of^[15] has evaluated the friction coefficient of spinning circular cylinders. The results of studies in^[15] show that the frictional torque coefficient (C_Q) may attain its minimum for the spinning range of $0.5 \leq \dot{\omega} \leq 1.5$ and at $1.7 \times 10^4 \leq Re$. But, at the prescribed range of the Reynolds numbers and spinning ratios, the drag to lift ratios are considerably high, *i.e.* $1.0 \leq C_D/C_L \leq 2.5$. Fig. 5 shows that the

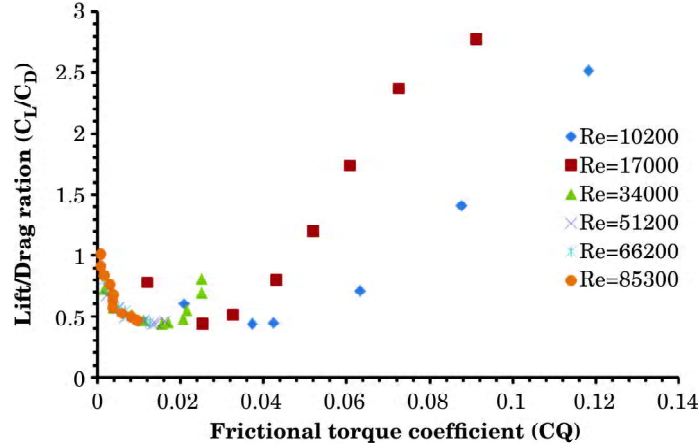


Fig. 5: Lift to drag ratio against frictional torque coefficient for the spinning circular cylinder (experiments of^[15])

frictional torque coefficient remains under the value of 0.05 if the lift to drag value passes low values of $0.5 \leq C_L/C_D \leq 1.0$.

More experimental or numerical results are needed to find an optimum range for the spinning ratio and the Reynolds number; however as a conclusion, we may suggest the range of spinning ratio to $1.5 \leq \dot{\omega} \leq 2.5$ and the Reynolds number within $1.7 \times 10^4 \leq Re \leq 3.4 \times 10^4$ for designing a better Magnus type wind turbine with cylindrical blades.

2. MATHEMATICAL MODELLING OF INVISCID FLOW

2.1. Potential Flow Solution

Considering incompressible, inviscid, and irrotational fluid flows around spinning cylinders, the continuity equation can be expressed as Laplace equation of the velocity potential, ϕ , for which the solution is referred as the potential flow. The velocity potential can be obtained for flows around aerodynamic bodies by combining the simple ideal flows known as elementary flows which are known as uniform flow, source and sink, doublet, and vortex flows. For the spinning cylinders, the potential flow may be constructed by superposition of the velocity potentials of three elementary flows; *i.e.* uniform flow, doublet at the centre of the cylinder, and vortex. In two dimensions, the velocity potential for the flow around the spinning cylinder is obtained as^[16].

$$\phi = U_{\infty} r \left(1 + \frac{r_c^2}{r^2} \right) \cos \theta - \frac{\Gamma}{2\pi} \theta \quad (3)$$

In which U_∞ is the uniform freestream velocity, r_c is the radius of the circular cylinder, Γ is the clockwise circulation for clockwise spin of the cylinder, and (r, θ) are the radial and angular coordinates from the centre of cylinder in cylindrical coordinate system. The velocity components for flowfield around the spinning cylinder is then calculated by

$$u_r = \frac{\partial \phi}{\partial r} = U_\infty \left(1 - \frac{r_c^2}{r^2}\right) \cos \theta \quad (4)$$

$$u_\theta = \frac{1}{r} \frac{\partial \phi}{\partial \theta} = -U_\infty \left(1 + \frac{r_c^2}{r^2}\right) \sin \theta - \frac{\Gamma}{2\pi r} \quad (5)$$

From equations (4) and (5), it is seen that on the surface of the spinning cylinder ($r = r_c$), the radial velocity is $u_r = 0$ and the tangential velocity is simplified to

$$u_\theta = -2U_\infty \sin \theta - \frac{\Gamma}{2\pi r_c} \quad (6)$$

The pressure, p , on the surface of cylinder is then determined from the Bernoulli equation and using the tangential velocity on (6), as follows

$$p_\infty + \frac{1}{2} \rho U_\infty^2 = p + \frac{1}{2} \rho \left(-2U_\infty \sin \theta - \frac{\Gamma}{2\pi r_c}\right)^2 \quad (7)$$

or

$$p = p_\infty + \frac{1}{2} \rho U_\infty^2 \left(1 - 4 \sin^2 \theta - \frac{2\Gamma \sin \theta}{\pi r_c U_\infty} - \frac{\Gamma^2}{4\pi^2 r_c^2 U_\infty^2}\right) \quad (8)$$

Since the inviscid flow solution is sought, there is no viscous shear and only the surface pressure is integrated around the spinning cylinder to obtain the drag and lift forces as follow:

$$F_L = F_y = - \int_0^{2\pi} \Delta p \sin \theta r_c d\theta = \rho U_\infty \Gamma \quad (9)$$

$$F_D = F_x = - \int_0^{2\pi} \Delta p \cos \theta r_c d\theta = 0 \quad (10)$$

The calculation above clearly shows that the drag force equals to zero hence it correct value cannot be obtained from this simple potential flow analysis. The lift force is seen as a linear increasing function of the freestream velocity U_∞ and the circulation Γ around the cylinder for an incompressible inviscid flow. The lift and drag coefficients are then defined as:

$$C_L = \frac{F_L}{\frac{1}{2}\rho U_\infty^2 A} \quad (11)$$

$$C_D = \frac{F_D}{\frac{1}{2}\rho U_\infty^2 A} \quad (12)$$

where A is a reference area, usually taken as the projected perpendicular area. For the two dimensional cylinder studied here, the reference area equals to diameter times the unit length of the cylinder; *i.e.*, $A = 2r_c$.

2.2. Actuator Disk Model for Rotor of Wind Turbine

The actuator disk model is a simplified model for the rotor of a horizontal axis wind turbine that the rotor is assumed with infinite number of blades (here rotating circular cylinders) with nears zero thickness of blades. In fact, the actuator disk model is the mathematical representation of the wind turbine rotor which assumes a sudden drop in pressure with continuous air speed across of the rotor area^[17]. The wind turbine is then modelled using an expanding stream tube encountered with the actuator disk and the air flow to be one-dimensional. Thus as shown in Fig. 6, the one dimensional momentum theory in the axial direction of the stream tube is used to analysis the linear momentum of air flow through the rotor area of the wind turbine.

Since the mass flow rate within the stream tube is conserved, the mass flow rate must be unchanged everywhere within the stream tube and is given by:

$$\dot{m} = \rho A_\infty U_\infty = \rho A_d U_d = \rho A_w U_w \quad (13)$$

The subscripts ∞ , d , and w refers to the free stream condition, flow condition at the actuator disc, and far wake flow condition; respectively.

The actuator disc induces velocity components in both axial and tangential directions. This should be considered for determining the relative wind speed across the blade sections. The axial part of the induced flow at the actuator disc is determined by product of an axial induction factor, a , and the free stream speed; *i.e.* $-aU_\infty$. Hence, the net axial velocity at the disk is determined by:

$$U_d = U_\infty(1 - a) \quad (14)$$

Considering the clockwise spinning cylinders of the Magnus wind turbine, the flow particles on top of the cylinders are accelerated while the flow particles at the bottom of the cylinders are decelerated. Therefore, both the effects of wake rotation and spin of blades should be accounted in

determining the induced velocity in tangential direction. This is discussed in full details next.

2.2.1. Conservation law for momentum of a stream tube

For the one-dimensional stream tube shown in Fig. 6, the conservation law of linear momentum is expressed as the rate of change of momentum of the air that passes through the actuator disc should be equal to the net forces causing this change. The mass flow rate times the overall change of velocity, $U_\infty - U_w$, gives the rate of change of momentum, *i.e.*, $\rho A_d U_d (U_\infty - U_w)$. Here, U_w is the air speed downstream of the actuator disc in the wake region. The net force causing this change comes merely from the pressure drop across the actuator disc; hence by using equation (14), the Newton's second law for the linear momentum is given as:

$$(p_d^+ - p_d^-)A_d = \rho A_d U_\infty (1 - a)(U_\infty - U_w) \quad (15)$$

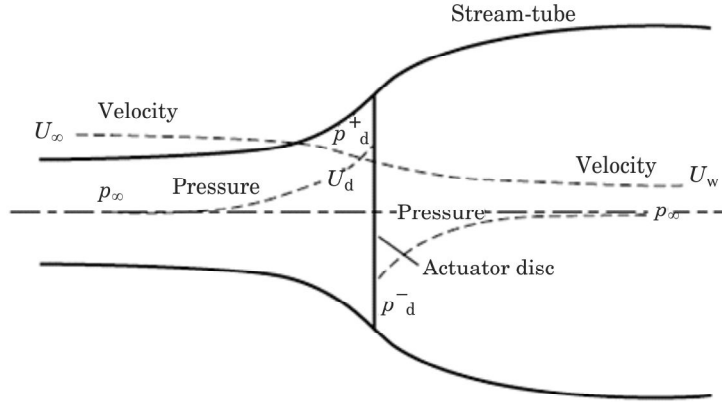


Fig. 6: The stream tube with actuator disk model for a horizontal axis wind turbine^[17]

Bernoulli's equation^[17] is applied on the upstream and downstream sections of the stream-tube to determine the pressure drop, $(p_d^+ - p_d^-)$, as follows:

$$(p_d^+ - p_d^-)A_d = \frac{1}{2} \rho (U_\infty^2 - U_w^2) \quad (16)$$

The equations (15) and (16) are equal so that the air stream downstream of the actuator disk in the wake region is determined by:

$$U_w = U_\infty (1 - 2a) \quad (17)$$

Hence, the net force of wind on the actuator disk using the equation (15) is calculated as

$$F = (p_d^+ - p_d^-)A_d = 2\rho A_d U_\infty^2 a(1 - a) \quad (18)$$

The rate of work done by the force on the actuator disk, FU_d , is equals to the power extracted from the wind; hence, the net power capture of the wind turbine is determined by

$$P = FU_d = 2\rho A_d U_\infty^3 a(1 - a)^2 \quad (19)$$

The power coefficient, the important parameter on performance of any wind turbine, is defined and determined as follows:

$$C_p = \frac{P}{\frac{1}{2}\rho U_\infty^3 A_d} = 4a(1 - a)^2 \quad (20)$$

Based on the Betz theory^[17], an ideal wind turbine at its best performance reduces wind speed to two third of the freestream value. Hence, the maximum value of the power coefficient is calculated using equation (20) by

implementing the optimum value of axial induction factor, *i.e.*, $a = \frac{1}{3}$. The corresponding with turbine attains its maximum power coefficient of

$C_{p_{max}} = \frac{16}{27} = 0.593$. This is also known as the Betz limit that no practical wind turbines can exceed this maximum level.

2.2.2. Conservation law for moment of momentum of a stream tube

As shown in Fig. 7, the conservation of moment of momentum must be satisfied so that the wind turbine produces a useful torque for generating power. This is done by using a wake rotation downstream of the rotor in some annular control volumes.

There is a connection between the loss of the linear momentum and the loss of moment of momentum or angular momentum. As flow passes through the rotor of wind turbine, a torque on the rotor disc is exerted by the air. To sustain the conservation of moment of momentum in the stream tube, an equal and opposite torque is required to be applied to air. This reaction torque causes that air rotates in opposite direction of the rotor and gains angular momentum. The air particles then possess axial and tangential velocity components. For the Magnus type rotors, an additional tangential velocity is created because of the spin of the cylinder. These velocity components are shown in Fig. 8 for the air particles passing through the

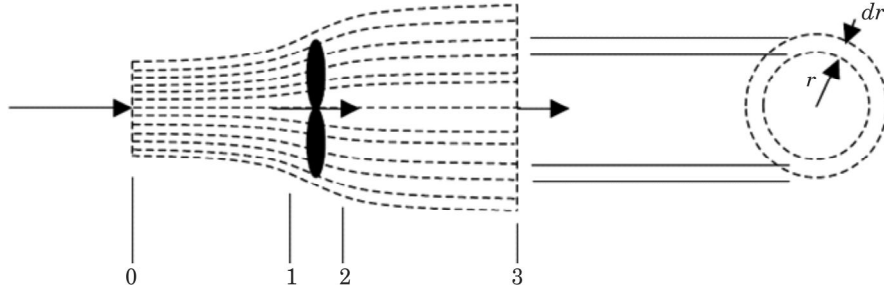


Fig. 7: Differential annular control volumes to study the wake rotation

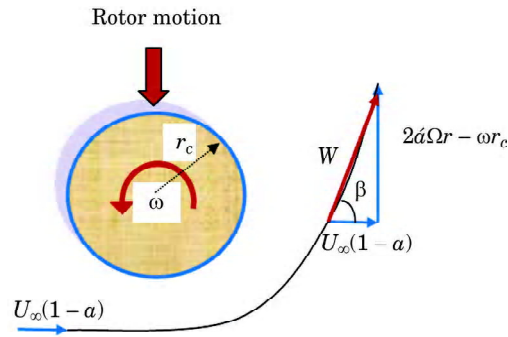


Fig. 8: The air velocities up and just downstream of the actuator disk

cylinder. To model the change in tangential velocity, the angular induction factor \hat{a} is used.

As shown in **Fig. 8**, assume that the rotor of Magnus blades is spinning circular cylinders with the cross sectional radius r_c and the rotational speed of ω along its axis. Considering a uniform axial inflow, the tangential velocity constitute of two parts in vicinity downstream of the actuator disc. One part is made of the blade angular movement in the plane of rotor, *i.e.* $2\hat{a}\Omega r$, in which Ω is the rotor angular velocity and r is the radial distance from the hub of wind turbine (the axis of rotation of rotor). Second part represents the wake reaction to the induced tangential velocity created by spin of each cylinder, *i.e.* ωr_c . This is the main difference between the Magnus type and the conventional aerofoil type wind turbines (see **Fig. 8**). Hence just slightly downstream of the actuator disk, the air axial velocity component is given by $U_\infty(1-\hat{a})$ and the tangential velocity component is determined by $2\hat{a}\Omega r - \omega r_c$. It is also generally assumed that on the actuator disc plane on the blade itself, the tangential velocity component is equals half the value of the same just downstream of the wind turbine, *i.e.* $\Omega r \hat{a} - \frac{\omega r_c}{2}$, in the same direction of rotor motion.

Consider the torque exerted by the annular section of the actuator disk on air as shown in Fig. 7 at the radius r with differential thickness of dr . The torque is equals to the rate of change of moment of momentum of the air passing through the annular section. Thus, the torque of the segment is equals to product of the mass flow rate through the annular section, the change of tangential velocity, and the radius of the annular section as follow

$$\delta Q = \rho \delta A_d U_\infty (1 - a) (2\Omega \dot{a} r - \omega r_c) r \quad (21)$$

Here δA_d is the area of the annular ring, δQ is the driving torque on the rotor shaft. The corresponding output shaft power is then determined by

$$\delta P = \Omega \delta Q = \rho \delta A_d U_\infty (1 - a) (2\Omega^2 \dot{a} r^2 - \omega \Omega r_c r) \quad (22)$$

The equation (19) from the linear momentum is employed for the annular ring, shown in Fig. 7, and is equated with the results obtained from the moment of momentum in equation (22) as follows

$$2\rho \delta A_d U_\infty^3 a (1 - a)^2 = \rho \delta A_d U_\infty (1 - a) (2\Omega^2 \dot{a} r^2 - \omega \Omega r_c r) \quad (23)$$

or in simpler form

$$2U_\infty^2 a (1 - a) = 2\Omega^2 \dot{a} r^2 - \omega \Omega r_c r \quad (24)$$

Defining the dimensionless parameters as the blade speed ratio, $\lambda_r = \frac{r\Omega}{U_\infty}$, and the cylinder spin ratio, $\dot{\omega} = \frac{r_c \omega}{U_\infty}$, a relation is found among the axial induction factor, the angular induction factor, and the spin ratio as follow

$$a(1 - a) = \lambda_r^2 \dot{a} - \frac{\dot{\omega}}{2} \lambda_r \quad (25)$$

The angular induction factor is then determined by rearranging equation (25) as follow:

$$\dot{a} = \frac{1}{\lambda_r^2} \left[a(1 - a) + \frac{\dot{\omega}}{2} \lambda_r \right] \quad (26)$$

The variation of the angular induction factor against the blade speed ratio at different values of the spin ratio, $\dot{\omega}$, using the optimum value of the axial induction factor, *i.e.*, $a = \frac{1}{3}$, is shown in Fig. 9. As shown in Fig. 9, the angular induction factor is a decreasing function of λ_r and also an increasing function of the spin ratio, $\dot{\omega}$.

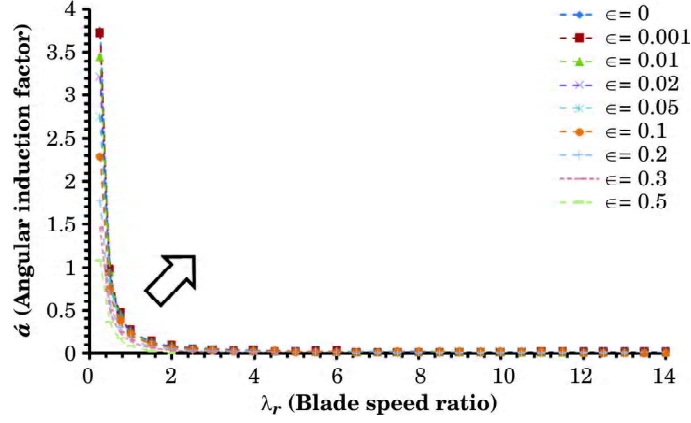


Fig. 9: Angular induction factor versus blade speed ratio at different spin ratios

The differential power given in equation (22) is rewritten using equation (26) as follows:

$$\delta P = \left(\frac{1}{2}\rho U_\infty^3 2\pi r dr\right) 4(1-a) \left(\lambda_r^2 \dot{a} - \frac{\dot{\omega}}{2}\lambda_r\right) \quad (27)$$

In dimensionless form, the power coefficient is given by

$$\frac{dC_p}{dr} = \frac{\delta P/dr}{\frac{1}{2}\rho U_\infty^3 \pi R^2} = \frac{4\pi\rho U_\infty^3 (1-a)r \left(\lambda_r^2 \dot{a} - \frac{\dot{\omega}}{2}\lambda_r\right)}{\frac{1}{2}\rho U_\infty^3 \pi R^2} \quad (28)$$

Using the dimensionless parameter $\mu = \frac{r}{R}$ with R defined as the tip radius of the blade from hub, the differential power coefficient with respect to μ is given as

$$\frac{dC_p}{d\mu} = 8(1-a) \left(\mu^3 \lambda^2 \dot{a} - \frac{\dot{\omega}}{2}\mu^2 \lambda\right) \quad (29)$$

For the optimum value of the induction factor, *i.e.* $a = \frac{1}{3}$, it is proved that the maximum power extraction from the wind turbine is similar to the case with non-rotating wake condition^[17]. Hence, equation (26) in form of

$\dot{a} = \frac{1}{\lambda^2 \mu^2} \left[\frac{2}{9} + \frac{1}{2}\dot{\omega}\lambda\mu\right]$ is substituted in the relation (29) and is integrated

along the rotor radius. For all values of $\dot{\omega}$ and λ , it is interestingly to note that the wind turbine produces the maximum power at the Betz limit, *i.e.*

$$C_p = \int_0^1 8(1-a) \left(\mu^3 \lambda^2 \acute{a} - \frac{\acute{\omega}}{2} \mu^2 \lambda \right) d\mu = \int_0^1 \frac{32}{27} \mu d\mu = \frac{16}{27} \quad (30)$$

This is consistency with the findings for the commercial aerofoil type wind turbines on not violating the Betz limit. Hence, the maximum power capture from the Magnus type wind turbine is obtained by using the optimum values for a and \acute{a} discussed above.

3. MATHEMATICAL MODELLING FOR BLADE ELEMENTS

3.1. Blade Element Modelling of the Magnus Rotor

In actuator disk modelling, the fluid flow is assumed inviscid and therefore the frictional drag is neglected which is not realistic. To modify this non-realistic assumption somehow^[17], the blade element modelling is used in which the effects of drag force is considered as a two-dimensional fluid flow over blade elements as shown in Fig. 10. In reality, the fluid flow across the blade is three dimensional; however, the aforementioned treatment is used to improve the inviscid modelling. Moreover, these three dimensional behaviour cause the generation of rotational kinetic energy in the wake, which resulted in less energy extraction by the rotor than it would be anticipated without wake rotation.

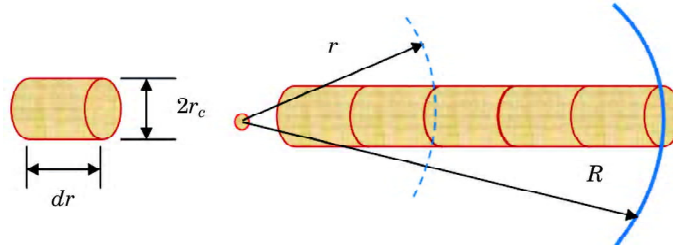


Fig. 10: Blade elements of a Magnus type cylindrical blade

For the blade element modelling, it is assumed that the forces acting on the blade elements are two dimensional lift and drag forces obtained from experimental measurements. Considering the air velocity components over the blade section, the relative wind angle, ϕ , of the resultant velocity is defined on the plane of the element as sketched in Fig. 11. Here, the three-dimensional effects and the velocity component in the radial direction due to centrifugal forces are ignored.

In order to extract the correct lift and drag forces values and their direction on each element, the resultant velocity and the corresponding inflow angle on the plane of the element at the radial distance of r should

be determined. As seen in Fig. 11, the resultant velocity is a function of the free stream wind speed, the axial and angular induction factors, the rotational speed of the rotor, and the spin of the cylinder itself. The values of the lift and drag coefficients are obtained from available experimental results or by inviscid analysis to be discussed in the subsection 2.3.1 together with some correlations to relate the drag force to the lift force.

Consider a Magnus type horizontal axis wind turbine which has B rotating circular cylinders and each cylindrical blade has the radius of r_c and the length (tip radius) of R . In the conventional aerofoil type horizontal axis wind turbines, both the chord length and the pitch angle may vary along the blade span. However, for the Magnus type wind turbines with cylindrical blades, the chord length (or cylinder diameter $2r_c$) may be fixed along the blade. Consider a Magnus rotor which operates at the angular velocity of Ω , with spinning speed of ω , and the wind speed of U_∞ . On the blade section as discussed, the tangential velocity comprises of the rotor tangential velocity $r\Omega$, the tangential velocity of wake $\acute{a}r\Omega$, and half the value of the spinning speed of cylinder $(\omega r_c)/2$, i.e. $(1 + \acute{a})r\Omega - (\omega r_c)/2$. The velocity components on the blade section of the Magnus type wind turbine and the corresponding lift and drag forces are shown in Fig. 11.

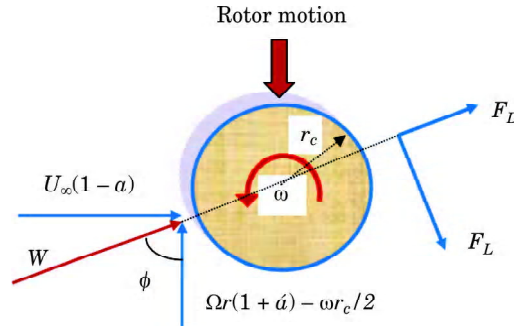


Fig. 11: The wind velocity and force components over the Magnus blade section

Here as shown in Fig. 11, the resultant relative velocity on the blade section is given by

$$W = \sqrt{U_\infty^2(1-a)^2 + ((1 + \acute{a})r\Omega - \omega r_c/2)^2} \quad (31)$$

As shown in Fig. 11, the relative wind angle with the plane of rotor motion is determined by

$$\phi = \tan^{-1} \left(\frac{U_\infty(1-a)}{(1 + \acute{a})r\Omega - \omega r_c/2} \right) = \tan^{-1} \left(\frac{1-a}{(1 + \acute{a})\lambda_r - \acute{\omega}/2} \right) \quad (32)$$

Here, $\lambda_r = \frac{r\Omega}{U_\infty}$ is the blade local speed ratio. By substituting the angular induction factor from the equation (26) into the relation (32), the relative wind incidence angle ϕ is expressed by an independent function of spin ratio as follows

$$\phi = \tan^{-1} \left(\frac{1-a}{\lambda_r + \frac{a(1-a)}{\lambda_r}} \right) = \tan^{-1} \left(\frac{\lambda_r(1-a)}{\lambda_r^2 + a(1-a)} \right) \quad (33)$$

For the optimum Magnus wind turbine with the optimal value of the axial induction factor, *i.e.* $a = \frac{1}{3}$, the unique distribution of the incidence angle ϕ is obtained as plotted in Fig. 12. Fig. 12 indicates that the relative wind angle attain its maximum at the blade speed ratio of nearly 0.5 with the approximate value of 35 degrees. Employing BEM analysis, the distribution of the relative wind incidence angle ϕ is modified later to incorporate the viscous effects to the above inviscid analysis.

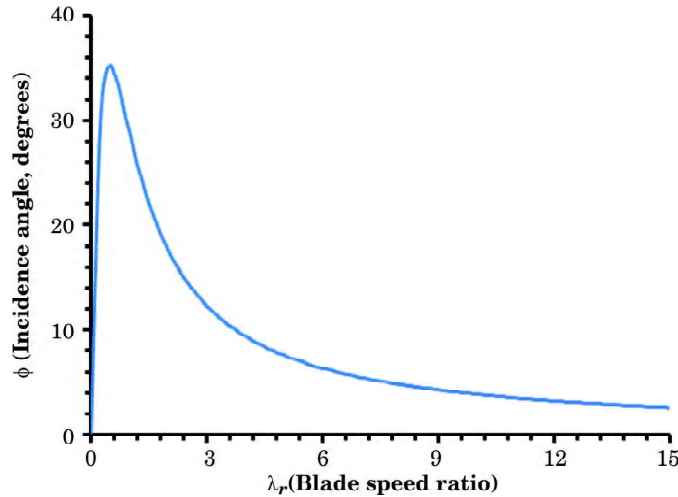


Fig. 12: The relative wind incidence angle across the blade sections of Magnus wind turbine with respect to the blade local speed ratio using inviscid momentum theory

Note that at the above analysis employ no restriction on the local blade radius r_c and its variation depends on the spin ratio, ω . To find the forces acting on blades as shown in Fig. 11, the tangential force F_T , which generates

the rotor torque, and the normal force F_N , which contribute to the rotor thrust force, are determined as

$$\begin{aligned} F_T &= F_L \sin \phi - F_D \cos \phi \\ F_N &= F_L \cos \phi + F_D \sin \phi \end{aligned} \quad (34)$$

Knowing the distribution of the relative wind angle from equation (33), the lift F_L and the drag F_D forces should be determined from experiments or analyses such as the potential flow solution, discussed next, or from the blade element momentum theory (BEM) which is discussed in section 3.4.

3.2. Potential Flow Solution to the Magnus Rotor

Using the Bernoulli equation, the pressure differences between the freestream and a point on the cylinders of the Magnus rotor can be determined by

$$\begin{aligned} \Delta p &= \frac{1}{2} \rho U_\infty^2 \left[1 - \frac{u_\theta^2}{U_\infty^2} \right] \\ u_\theta &= -2W \sin \left(\theta + \frac{\pi}{2} - \phi \right) + r_c \omega \end{aligned} \quad (35)$$

Here, u_θ is the tangential component of velocity on the surface of the spinning cylinder composed of the tangential part of freestream velocity on the surface and the spin velocity of the cylinder. The term $\frac{u_\theta^2}{U_\infty^2}$ can be expressed as by substituting W and ϕ from equations (31) and (32) to give

$$\begin{aligned} \frac{u_\theta^2}{U_\infty^2} &= \left(\omega - 2X \sin \left(\theta + \frac{\pi}{2} - \phi \right) \right)^2 \\ X &= \frac{W}{U_\infty} = (1 - a) \sqrt{1 + \cot^2 \phi} \end{aligned} \quad (36)$$

Hence, the lift and drag forces as defined by equations (9) and (10) are modified for the Magnus rotor as follows

$$F_L = - \int_0^{2\pi} \Delta p \sin \left(\theta + \frac{\pi}{2} - \phi \right) r_c d\theta \quad (37)$$

$$F_D = - \int_0^{2\pi} \Delta p \cos \left(\theta + \frac{\pi}{2} - \phi \right) r_c d\theta \quad (38)$$

Employing the pressure difference from (35) and the lift and drag coefficients definitions in (11) and (12), one may obtain the following relations on lift and drag coefficients for the Magnus rotor

$$C_L = \frac{F_L}{\frac{1}{2}\rho U_\infty^2 A} = \frac{1}{2} \int_0^{2\pi} \left[1 - \left(\dot{\omega} - 2X \sin\left(\theta + \frac{\pi}{2} - \phi\right) \right)^2 \right] \sin\left(\theta + \frac{\pi}{2} - \phi\right) d\theta$$

$$= \frac{\pi \dot{\omega}}{\lambda_r} \sqrt{4\lambda_r^4 + 4\dot{\omega}\lambda_r^3 + 4(1 - a^2 + \dot{\omega}^2)\lambda_r^2 + 4a\dot{\omega}(1 - a)\lambda_r + 4a^2(a - 1)^2} \quad (39)$$

$$C_D = \frac{F_D}{\frac{1}{2}\rho U_\infty^2 A} = -\frac{1}{2} \int_0^{2\pi} \left[1 - \left(\dot{\omega} - 2X \sin\left(\theta + \frac{\pi}{2} - \phi\right) \right)^2 \right] \cos\left(\theta + \frac{\pi}{2} - \phi\right) d\theta = 0 \quad (40)$$

The above solution to the lift coefficient is dependent on the blade speed ratio, λ_r , the axial induction factor, a , and the dimensionless spin ratio, $\dot{\omega}$.

Using the optimum value of induction factor across the blade, *i.e.* $a = \frac{1}{3}$, the distribution of the lift coefficient are plotted in Fig. 13 against λ_r at different values of $\dot{\omega}$. It is seen that the lift coefficient is a nonlinear function of the blade speed ratio, λ_r , below unity; however, it maintain a linear increase for larger values of λ_r . The spinning speed or changes in magnitude of the chord of blade is combined in the rotational speed $\dot{\omega}$ which shows an increasing effect on lift coefficient with respect to the local blade speed

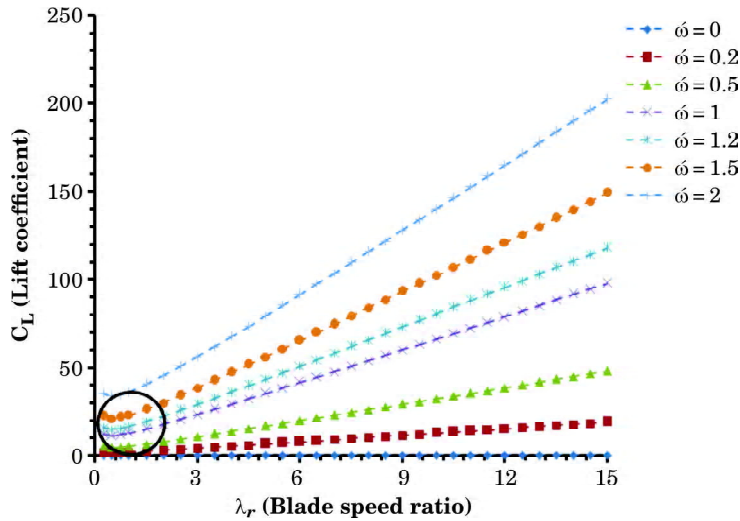


Fig. 13: The distribution of lift coefficient along the Magnus blade versus the blade speed ratio at different spin ratios using the inviscid momentum theory

ratio, λ_r . Results on the two-dimensional spinning circular cylinder for the lift force $\rho U_\infty \Gamma$ shows that the lift force magnitude and direction are constant along cylinder for a given wind speed and spin. However for the Magnus

rotor, the relative wind speed $W = \sqrt{U_\infty^2(1-a)^2 + ((1+a)r\Omega - \omega r_c/2)^2}$ is increased along the blade and its direction is also changed; therefore, the lift coefficient changes both magnitude and direction along the rotor blade from root to tip. Hence, the larger aspect ratio of the blade yields the higher values of the lift force. From this potential analysis, it is also seen that the spin of rotor can considerably increase the lift force towards the tip of the Magnus blade. However as expected from this inviscid analysis, the zero value for drag coefficient is obtained.

3.3. Blade Element Momentum (BEM) Theory for the Magnus Rotor

The combination of the blade element and momentum theory is referred as the BEM theory. In BEM theory, the fluid flow over blade sections is assumed two dimensional. This means that the two-dimensional lift and drag forces on a blade element are responsible for the change of momentum of the air passing through the annular area that is swept by the rotor element as shown in Fig. 7. Therefore, the radial components of velocity and force interact between the flow and the rotor is ignored. This is acceptable if the axial flow induction factor remain constant in radial direction. In practice, there are conditions that confirm validity of this assumption (see^[17]) in most part of blade except near to root and tip of blades.

Consider a Magnus wind turbine with a rotor comprising B blades of rotating circular cylinders, the differential axial force, dF_N , acting on the blade element, dr , on all B number of blades, is obtained dF_N ing equation (34), (11), and (12) as follows

$$dF_N = dF_L \cos \phi + dF_D \sin \phi = \frac{1}{2} \rho W^2 B (2r_c dr) (C_L \cos \phi + C_D \sin \phi) dr \quad (41)$$

In which, the two-dimensional area $2r_c dr$ is assumed as the reference area. As discussed in section 2.2.1 for the linear momentum theory on the actuator disk, the differential axial force in equation (41) is also equals to the rate of change of axial momentum of the air passing through the swept annulus, shown in Fig. 7, as follow

$$dF_N = (p_d^+ - p_d^-) dA_d = 4\pi \rho U_\infty^2 a(1-a) r dr \quad (42)$$

The pressure drop across the actuator disk has also extra components here due to the wake rotation and the spin of cylinder which contribute to the drop in the wake pressure by increasing in dynamic head. This is defined

based on the tangential velocity just downstream the actuator disk as follows

$$\frac{1}{2}\rho(2\acute{\alpha}\Omega r - \omega r_c)^2$$

Thus, the extra dynamic head of air on the annular swept area is determined by

$$\frac{1}{2}\rho(2\acute{\alpha}\Omega r - \omega r_c)^2 dA_d = \pi\rho(2\acute{\alpha}\Omega r - \omega r_c)^2 r dr$$

Hence by combining the relations (41) and (42) for the differential, one can obtain

$$\frac{1}{2}\rho W^2 B(2r_c)(C_L \cos \phi + C_D \sin \phi) dr = 4\pi\rho \left[U_\infty^2 a(1-a) + \frac{1}{4}(2\acute{\alpha}\Omega r - \omega r_c)^2 \right] r dr \quad (43)$$

By some arithmetic manipulations, the relation (43) is rewritten as

$$\frac{W^2}{U_\infty^2} B \left(\frac{2r_c}{R} \right) (C_L \cos \phi + C_D \sin \phi) = \frac{8\pi r}{R} \left[a(1-a) + \frac{1}{4U_\infty^2} (2\acute{\alpha}\Omega r - \omega r_c)^2 \right] \quad (44)$$

The tangential force given in equation (34) is responsible for the generation of the torque across the blade, $\delta Q = r dF_T$. Also from the linear momentum equation (21), the differential torque of a blade element is determined. Hence by equating these two relations, the following relation is obtained

$$\begin{aligned} \delta Q = r dF_T &= \frac{1}{2}\rho W^2 B(2r_c)(C_L \sin \phi - C_D \cos \phi) r dr \\ &= 2\pi\rho U_\infty(1-a)(2\Omega \acute{\alpha} r - \omega r_c) r^2 dr \end{aligned} \quad (45)$$

By some arithmetic manipulations, the relation (45) is rewritten as

$$\frac{W^2}{U_\infty^2} B \left(\frac{2r_c}{R} \right) (C_L \sin \phi - C_D \cos \phi) = \frac{4\pi r}{RU_\infty} (1-a)(2\Omega \acute{\alpha} r - \omega r_c) \quad (46)$$

Dividing equations (44) and (46), one can obtain

$$\frac{C_L \cos \phi + C_D \sin \phi}{C_L \sin \phi - C_D \cos \phi} = \frac{\frac{8\pi r}{R} \left[a(1-a) + \frac{1}{4U_\infty^2} (2\acute{\alpha}\Omega r - \omega r_c)^2 \right]}{\frac{4\pi r}{RU_\infty} (1-a)(2\Omega \acute{\alpha} r - \omega r_c)} \quad (47)$$

Using dimensionless parameters and defining the drag to lift ratio $\epsilon = C_D/C_L$, one may obtain, after some manipulations, the following relation on the relative wind angle across the Magnus blade

$$\frac{1 + \epsilon \tan \phi}{\tan \phi - \epsilon} = \frac{2a(1-a) + \frac{1}{2}(2\acute{a}\lambda_r - \acute{\omega})^2}{(1-a)(2\acute{a}\lambda_r - \acute{\omega})} = \frac{2a}{(2\acute{a}\lambda_r - \acute{\omega})} + \frac{(2\acute{a}\lambda_r - \acute{\omega})}{2(1-a)} = Y \quad (48)$$

Taking the optimum value for the axial induction factor, *i.e.*, $a = 1/3$ and substituting \acute{a} from equation (26), the Y function above is simplified to

$$Y(\lambda_r) = \frac{1}{(1-a)}\lambda_r + \frac{a}{\lambda_r} \quad (49)$$

The Y function is a known function of the axial induction factor, a , and the blade speed ratio, λ_r . By obtaining the drag to lift ratio ϵ from experimental measurements, the relative wind angle over the rotor of the Magnus rotor in equation (48) is rewritten as

$$\tan \phi = \frac{1+Y\epsilon}{Y-\epsilon} \quad (50)$$

At the limit of inviscid solution, *i.e.* $\epsilon = 0$, the variation of the relative wind angle ϕ obtained from equation (50) is identical to the equation (33), which is

$$\phi = \tan^{-1}\left(\frac{1}{Y}\right) = \tan^{-1}\left(\frac{1-a}{\lambda_r + \frac{a(1-a)}{\lambda_r}}\right) \quad (51)$$

However to determine the relative wind angle, ϕ , for non-zero values of the drag to lift ratio, ϵ , it is required to determine the angular induction factor, \acute{a} . This is done by combining the relation (32) and the equation (50) as follow

$$\tan \phi = \frac{1 + Y\epsilon}{Y - \epsilon} = \frac{1 - a}{(1 + \acute{a})\lambda_r - \acute{\omega}/2} \quad (52)$$

By substituting $Y = \frac{2a}{(2\acute{a}\lambda_r - \acute{\omega})} + \frac{(2\acute{a}\lambda_r - \acute{\omega})}{2(1-a)}$ from (48) in equation (52) and some arithmetic manipulations, the angular induction factor, \acute{a} , in the form of a new parameter, Z , is deduced as a new cubic equation as follows

$$\begin{aligned}
pZ^3 + qZ^2 + sZ + t &= 0 \\
p &= \epsilon \\
q &= -2\epsilon\lambda_r \\
s &= \epsilon(1-a)^2 + \lambda_r(1-a) + \epsilon a(1-a) + \epsilon\lambda_r^2 \\
t &= -(1-a)^2(a + \epsilon\lambda_r) - (1-a)\lambda_r^2 \\
Z &= (1 + \hat{a})\lambda_r - \hat{\omega}/2
\end{aligned} \tag{53}$$

Interestingly from the equation (53), it is seen that all coefficients of this cubic equation are only dependant function of the axial induction, the drag to lift ratio, and the local speed ratio. The cubic equation may have three roots, *i.e.* Z_1 , Z_2 , and Z_3 , for which three solutions are obtained for the agular induction factor \hat{a} from the following relation

$$a' = -1 + \frac{Z + \hat{\omega}/2}{\lambda_r} \tag{54}$$

And more interestingly, the relative wind incidence angle ϕ is deemed to be independent from spin ratio, $\hat{\omega}$, as follows

$$\phi = \tan^{-1} \left(\frac{1-a}{Z} \right) \tag{55}$$

As seen in (53), Z is the root of the cubic equation in which all coefficients are independent of the spin ratio $\hat{\omega}$. The angular induction factor should be determined by finding the roots of the cubic equation (53) which is dependant to drag to lift ratio. Hence, the effects of viscosity appears on the angular induction factor and not on the axial induction factor based on the above discussed BEM analyses.

The cubic equation (53) may possess complex roots which are nonphysical and discarded. Having solved the cubic equation (53) with the optimal value of the axial induction factor; *i.e.* $a = 1/3$, and the constant spin ratio of $\hat{\omega} = 0.1$, the variation the angular induction factor are investigated for different values of the drag to lift ratio, ϵ , and the local speed ratio, λ_r . As seen in Fig. 14, the angular induction factor is a decreasing function of the blade speed ratio λ_r . It is also observed that the angular induction factor reduces by increasing the drag to lift ratios, ϵ , from the value of zero to 0.5. For higher drag to lift ratio of less interest in practical conditions, the angular induction factor may attain negative values which may not be physical and further experimental validation or analytical studies should reveal more insight into the physics of such conditions.

Based on the calculated angular induction factors shown in Fig. 14, it is expected that the results of the relative wind angle, shown in Fig. 12 at the

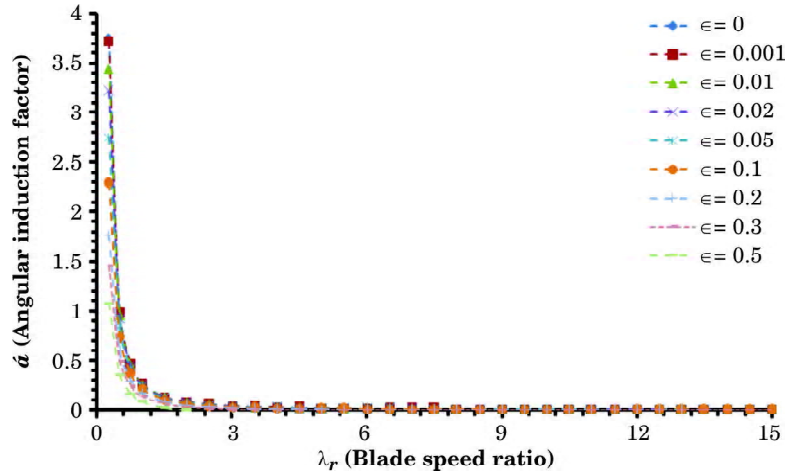


Fig. 14: The distribution of the angular induction factor at different values of the drag to lift ratio versus the blade local speed ratio using the BEM theory

case of inviscid flow $\epsilon = 0$, to be changed for this viscous case of the BEM theory.

The results in Fig. 15 for the relative wind angle clearly shows the same trend of decreasing function with respect to the blade speed ratio λ_r . By increasing the drag to lift ratio, it is observed that the relative wind incidence angle is marginally enhanced in the vicinity of low values of the blade speed ratio, λ_r , to the value of 3.

For the higher value of the dimensionless spin ratio, ω , the solutions to the cubic equation (53) were identical as proved by equation (55) and discussed.

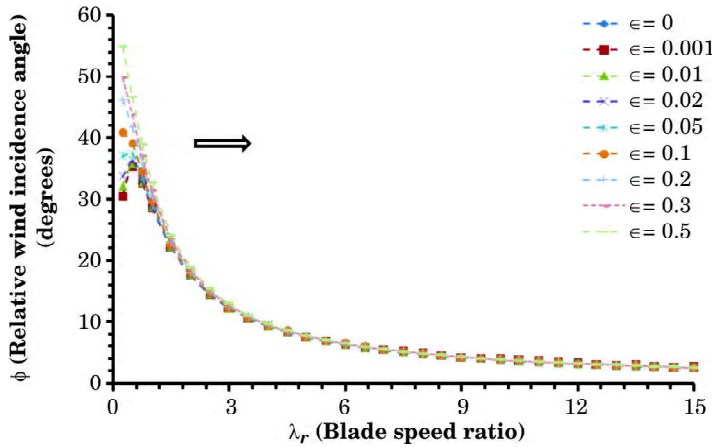


Fig. 15: The distribution of the wind incidence angle at different values of the drag to lift ratio versus the blade speed ratio using the BEM theory

This leads to identical relative wind angles as shown in Fig. 15 and therefore it can be claimed that the relative wind angle is independent function of the spin ratio; while, the angular induction factor is a monotonic increasing function of the spin ratio (see the equation 54).

In summary, it can be claimed that the spin ratio is not directly controlling the Magnus wind turbine performance through the relative wind incidence angle; but, it is more pronounced on the effects it has on the lift and drag of Magnus blades. Thus, the BEM analysis take into account the effects of the spin ratio only by altering the values of drag and lift forces at different spin ratios. It should be noted that the drag to lift ratio is assumed constant along the blade which is correct if the drag force grows with the same rate as the lift force increases along the blade from root to tip. This is realistically accurate because the spin ratio of the cylinder is constant and changes on Reynolds number across the blade due to increase of the relative wind speed from root to tip is negligible.

4. THE OPTIMUM POWER COEFFICIENT OF MAGNUS TYPE WIND TURBINES

The important characteristic of a wind turbine is the power performance and the amount of wind energy that can be extracted from wind. A local power coefficient, including the effects of drag force, may be defined for the annular element of rotor, $dA_d = 2\pi r dr$, as follows

$$C_{P_l} = \frac{\delta P}{\frac{1}{2}\rho U^3 dA_d} = \frac{\Omega \delta Q}{\frac{1}{2}\rho U_\infty^3 (2\pi r dr)} \quad (56)$$

To determine the power coefficient, the torque developed on an element of Magnus rotor at radial distance of r should be determined. Using BEM results on the relative wind angle, the torque is determined using equation (45) as follow

$$\delta Q = \frac{1}{2} \rho W^2 B(2r_c) (C_L \sin \phi - C_D \cos \phi) r dr \quad (57)$$

By some extensive arithmetic manipulations as described in^[17], the lift coefficient may be derived from the equation (44) as follows

$$r_c C_L = \left[a(1 - a) + \left(a\lambda_r - \frac{\dot{\omega}}{2} \right)^2 \right] \frac{U_\infty^2}{W^2} \left(\frac{4\pi r}{B} \right) \frac{1}{\cos \phi (1 + \epsilon \tan \phi)} \quad (58)$$

Substituting both equations (57) and (58) into equation (56), one may obtain the local power coefficient by some manipulations as follows

$$C_{p_l} = 4\lambda_r \left[a(1-a) + \left(\dot{a}\lambda_r - \frac{\dot{\omega}}{2} \right)^2 \right] \left[\frac{\tan \phi - \epsilon}{1 + \epsilon \tan \phi} \right] \quad (59)$$

Substituting \dot{a} from equation (54), the equation (59) can be rewritten as

$$C_{p_l} = 4\lambda_r [a(1-a) + (Z - \lambda_r)^2] \left[\frac{\tan \phi - \epsilon}{1 + \epsilon \tan \phi} \right] \quad (60)$$

As observed in the relation (60), the equation (53) on Z , and also the equation (55) on the relative wind incidence angle ϕ , the local power coefficient is independent function of the spin ratio; or in fact, it is not directly a dependent function of the spin ratio $\dot{\omega}$.

The total power gain from the wind turbine rotor defined in equation (61) may be integrated numerically from hub to tip radiuses to give the power coefficient for the rotor swept area at a prescribed tip speed ratio, λ , as follows

$$C_{p_{tot}} = \frac{2}{\lambda^2} \int_{\lambda_h}^{\lambda} \lambda_r C_{p_l} d\lambda_r = \frac{8}{\lambda^2} \int_{\lambda_h}^{\lambda} \lambda_r^2 \left[a(1-a) + \left(\dot{a}\lambda_r - \frac{\dot{\omega}}{2} \right)^2 \right] \left[\frac{\tan \phi - \epsilon}{1 + \epsilon \tan \phi} \right] d\lambda_r \quad (61)$$

The blade tip speed ratio is denoted by $\lambda = \frac{R\Omega}{U}$. The effects of root and tip loss corrections may also be implemented into the above analysis using the Prandtl correction factor, F .

Inserting the optimum values of the axial induction factor, $a = 1/3$, and $\phi = \tan^{-1} \left(\frac{1 + Y\epsilon}{Y - \epsilon} \right)$, the results of the local power distribution given by equation (60) is obtained and shown in Fig. 16. For any optional value of spin ratio $\dot{\omega}$, the same results as those shown in Fig. 16 are obtained for the local power coefficient at different values of drag to lift ratio versus the local speed ratio. It is interestingly to note that the local power coefficient for the ideal case of zero drag to lift ratio is independent from λ_r and is equals everywhere to the maximum value of Betz limit; *i.e.* $C_{p_l} = \frac{16}{27}$, which is valid theoretically.

The power coefficient shown in Fig. 16 only presents the power gain from wind regardless the power consumed by each spinning blades. In fact, the net power is subtract of these two powers; *i.e.* the power gain from wind minus the power consumed for spinning blades. In Fig. 16, the results of the present theory are compared with a typical experimental result of Komatinovic^[7] for a Savonius Magnus type wind turbines. Note that, the

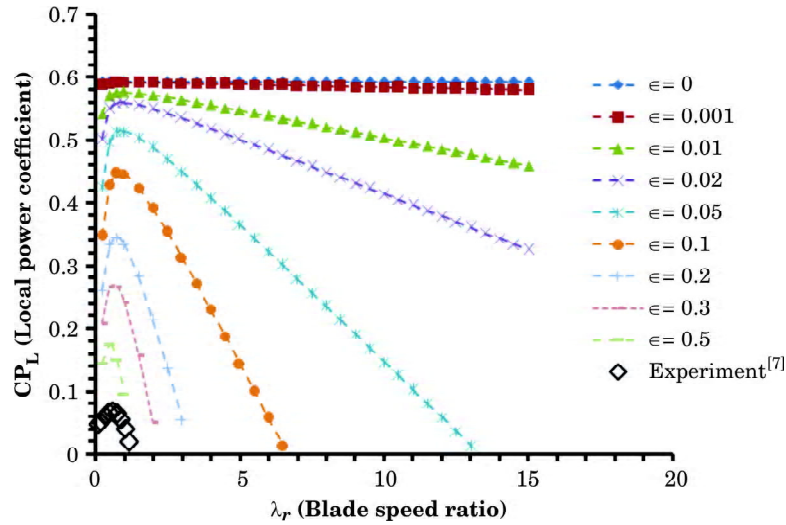


Fig. 16: The distribution of the local power coefficient at different values of the drag to lift ratio versus the blade speed ratio using the BEM theory (for any spin ratio)

finding of this study can equally be applied to any Magnus type wind turbines regardless of its blade cross sectional shape; whether cylindrical or non-cylindrical. The theory is also valid for non-uniform chord length and untwisted blade cross section shapes. As shown in Fig. 17, it is comparable to see that the Magnus blade generate the full power throughout the blade (see Fig. 16); while, the aerofoil type commercial wind turbine blades produces zero power near the root of blades^[18]. This superiority is another

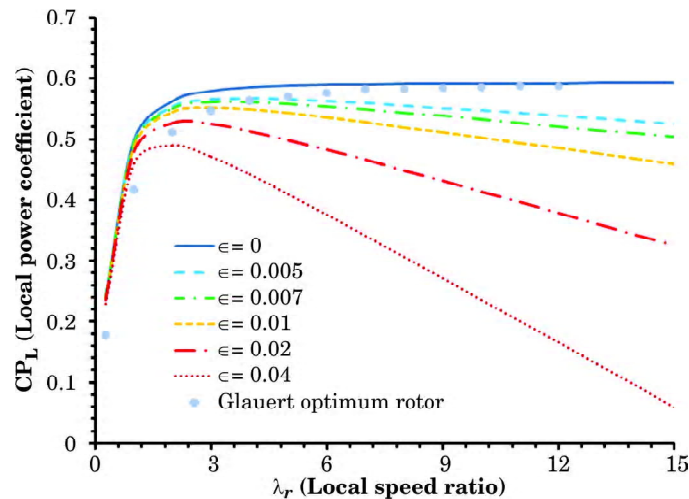


Fig. 17: The local power coefficient at different values of drag to lift ratio versus the local speed ratio for horizontal axis aerofoil type wind turbines^[18]

feature of the Magnus type wind turbines that can be related to the rotation of Magnus blade in comparison with fixed aerofoil blades.

Similar to the aerofoil type commercial wind turbines, reducing the parameter of drag to lift ratio of aerofoil cross sections is the most crucial task to enhance power capture of the wind turbine. As shown in Fig. 16, it is similarly the main challenge for the Magnus type horizontal axis wind turbines to reduce the drag to lift ratio.

5. THE CIRCULATING AEROFOIL-MAGNUS TYPE WIND TURBINE

It is usually misinterpreted the concept of Magnus effect as generation of high lift from spinning symmetrical geometries such as cylinders, spheres, or disks. However, the Magnus effect should be correctly intercepted as generating lift from circulating bodies with any aerodynamic shape. To proof this, the symmetrical NACA0015 aerofoil with treadmill like motion of its surface is computationally investigated. A schematic of the blade cross section with treadmill like motion (circulating) of its surface is shown in Fig. 18.

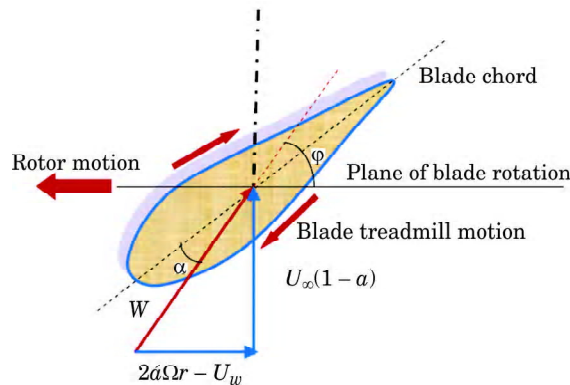


Fig. 18: The schematic of a treadmill like motion (circulating) of a blade section

The concept of Magnus force from any aerodynamic shape was actually invented by Anton Flettner in the year 1923 for aerofoils, which was granted by a German patent^[19]. However, to our knowledge to this date, no computational or experimental efforts were conducted on analysis and simulation of circulating aerofoils. For practical conditions, the simpler shapes as suggested by Flettner in Fig. 19 may be used; hence, to avoid costly experimental preparations and testing, it is worthwhile to assess computationally the merits and validity of using circulating aerofoils for application in aerofoil-Magnus type wind turbines. Note here that, it is not practical to alter chord length or twist angle along the blade of the aerofoil-

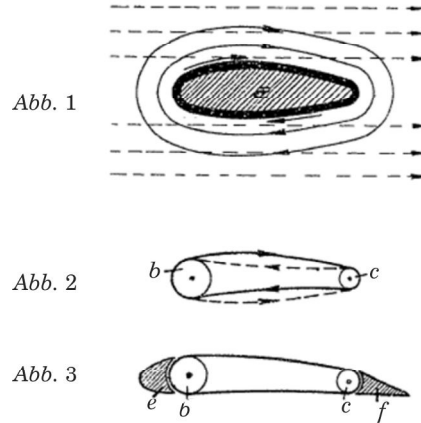


Fig. 19: The Magnus force by circulating aerofoil: (1) an ideal full circulating aerofoil; (2) a practical simpler treadmill system; (c) a more practical partial circulating aerofoil^[19].

Magnus type wind turbine. In fact, this can be advantageous which allows simpler and feasible manufacturing of blades.

To examine the merit of a circulating aerofoil and to assess lift generation at zero incidence angles, the symmetrical NACA0015 aerofoil is computationally investigated here. The aim is to evaluate the lift to drag ratio of circulating aerofoils for use in wind turbine blades. The BEM analysis explained in details in section 3, may be equally employed to the aerofoil-Magnus blades. However to examine the applicability of the aforementioned BEM analysis for use in the aerofoil-Magnus blades, some intensive computational and experiments are required to assess this and to find an optimum cross section of aerofoil-Magnus blades.

Here, the compressible two-dimensional flow solver developed by Sedaghat^[20] is used for solving viscous fluid flow around circulating aerofoils. The solver is based on a class of finite-volume, high resolution, and TVD schemes to solve the RANS equations of the fluid flow around aerofoils with the zero equation Baldwin-Lomax turbulence modelling. To solve the flow field around the circulating aerofoils, a C-type structured hyperbolic mesh was generated around the symmetrical NACA0015 aerofoil. Details of the boundary and initial conditions are explained in^[20]; however for the circulating aerofoil, the surface was allowed to move with a constant speed in clockwise direction. A dimensionless treadmill speed is then defined as the ratio of skin speed to the free stream speed. First, the symmetrical NACA0015 aerofoil is used as an example to assess if the lift force can be generated at zero incidence angles. Second, the lift to drag ratio is evaluated in comparison with a fixed aerofoil using different treadmill speeds.

5.1. Governing Fluid Flow Equations

Neglecting body forces and volumetric heating, the non-dimensional form of compressible Navier-Stocks equations in the transformed coordinate system for two dimensional flows can be written as

$$\frac{\partial \hat{U}}{\partial t} + \frac{\partial \hat{F}}{\partial \xi} + \frac{\partial \hat{G}}{\partial \eta} = 0 \quad (62)$$

where,

$$\begin{aligned} \hat{U} &= U/J \\ \hat{F} &= (\xi_x F + \xi_y G) / J, \quad \hat{G} = (\eta_x F + \eta_y G) / J \\ J &= \xi_x \eta_y - \xi_y \eta_x \end{aligned} \quad (63)$$

In the above, $\xi = \xi(x, y)$ and $\eta = \eta(x, y)$ are coordinate transformation function and J is the Jacobian of the transformation. The vectors U, F and G contains conserve variables or their fluxes and are given by

$$U = \begin{bmatrix} \rho \\ \rho u \\ \rho v \\ e \end{bmatrix}, F = \begin{bmatrix} \rho u \\ P + \rho u^2 - \tau_{xx} \\ \rho uv - \tau_{xy} \\ (e + P)u - u\tau_{xx} - v\tau_{xy} + q_x \end{bmatrix}, G = \begin{bmatrix} \rho v \\ \rho uv - \tau_{xy} \\ P + \rho v^2 - \tau_{yy} \\ (e + P)v - u\tau_{xy} - v\tau_{yy} + q_y \end{bmatrix} \quad (64)$$

Where ρ, u, v, e, q are density, velocity components along x, y directions, total energy and heat flux, respectively. ~~The components of shear stress and heat tensor are given as U is an array of conserved variables~~

The pressure, P , for a perfect gas as follows:

$$P = (\gamma - 1) \left[e - \frac{1}{2} \rho (u^2 + v^2) \right] \quad (65)$$

Where λ is the ratio of specific heats.

The components of stress tensor and the heat flux vector are as follow:

$$\begin{aligned} \tau_{xx} &= \frac{\mu}{\text{Re}} \left(\frac{4}{3} \frac{\partial u}{\partial x} - \frac{2}{3} \frac{\partial v}{\partial y} \right) \\ \tau_{yy} &= \frac{\mu}{\text{Re}} \left(\frac{4}{3} \frac{\partial v}{\partial y} - \frac{2}{3} \frac{\partial u}{\partial x} \right) \end{aligned}$$

$$\begin{aligned}
\tau_{xy} &= \frac{\mu}{\text{Re}} \left(\frac{\partial u}{\partial y} + \frac{\partial v}{\partial x} \right) \\
q_x &= \frac{-\mu\gamma}{(\gamma-1)\text{Re Pr}} \frac{\partial(p/\rho)}{\partial x} \\
q_y &= \frac{-\mu\gamma}{(\gamma-1)\text{Re Pr}} \frac{\partial(p/\rho)}{\partial y}
\end{aligned} \tag{66}$$

Where μ , Pr are Re the non-dimensional molecular viscosity, the Prandtl number, and the Reynolds number and are given by:

$$\begin{aligned}
\mu &= T^{3/2} \left(\frac{T_\infty^* + 110.4}{T^* + 110.4} \right) \\
\text{Pr} &= \frac{c_p^* \mu^*}{\kappa^*} \\
\text{Re} &= \frac{\rho_\infty^* U_\infty^* L^*}{\mu_\infty^*}
\end{aligned} \tag{67}$$

Where the superscript (*) represents dimensional quantities and L^* is a reference length usually taken as the aerofoil chord length. The non-dimensional static temperature is given by:

$$T = \gamma M_\infty^2 \frac{p}{\rho} \tag{68}$$

Where M_∞ is the freestream Mach number. For air and for laminar flows, the standard constant values of $\gamma = 1.4$ and $\text{Pr} = 0.72$ are used.

For turbulent flow computations, using a zero-equation model such as Baldwin-Lomax model, the time-averaged Navier-Stokes equations may be rewritten in the same format as the governing laminar-equations by replacing the transport coefficients by:

$$\begin{aligned}
\mu &= \mu_l + \mu_t \\
\frac{\kappa}{c_p} &= \frac{\mu_l}{\text{Pr}_l} + \frac{\mu_t}{\text{Pr}_t}
\end{aligned} \tag{69}$$

Where the turbulent Prandtl number Pr_t is assumed to be constant and is taken equals to 0.9 for air. The turbulent viscosity coefficient μ_t is determined from a turbulence model.

5.2. Numerical Algorithm

A class of implicit, second order accurate, total variation diminishing (TVD), and time-marching scheme has been adopted here for computation of two dimensional compressible flows. The method is based on upwind and symmetric TVD schemes reported by Yee and further modified by Sedaghat^[20] for computation of viscous flows. In this work, the upwind TVD method with the Van-Leer limiter function was selected due to better predictability in high gradient regions.

The Alternative Direction Implicit (ADI) form of Linearized Conservative Implicit (LCI) TVD scheme in generalized curvilinear coordinates $(\xi(x, y), \eta(x, y))$ are given by^[20]:

$$\begin{aligned} \left\{ I + \Delta t_{ij} \left(H_{i+1/2,j}^\xi - H_{i-1/2,j}^\xi \right) \right\} \frac{E^*}{J} &= \frac{RHS}{J} \\ \left\{ I + \Delta t_{ij} \left(H_{i,j+1/2}^\eta - H_{i,j-1/2}^\eta \right) \right\} \frac{E^n}{J} &= \frac{E^*}{J} \end{aligned} \quad (70)$$

with $J = \xi_x \eta_y - \xi_y \eta_x$ the Jacobian of transformation and $U^{n+1} = U^n + E^n$ where the superscript n and $n+1$ correspond to the previous and the next time steps. For steady-state applications a local time-stepping based on mesh Jacobian, $\Delta t_{i,j} = T / (1 + \sqrt{J_{i,j}})$, is used in which a typical value of the constant T is 0.3 for faster convergence.

The operators are defined as

The operators H^{eta} and H^{cisi} are defined as

$$\begin{aligned} H_{i,j\pm 1/2}^\eta E^n &= \frac{1}{2} \left[\hat{B}_{i,j\pm 1/2}^\eta E_{i,j\pm 1/2}^\eta - \Omega_{i,j\pm 1/2}^\eta E^n \right] \\ H_{i\pm 1/2,j}^\xi E^* &= \frac{1}{2} \left[\hat{A}_{i\pm 1/2,j}^\xi E_{i\pm 1/2,j}^* - \Omega_{i\pm 1/2,j}^\xi E^* \right] \end{aligned} \quad (71)$$

The Jacobian matrices $\hat{A} = \xi_x A + \xi_y B$ and $\hat{B} = \eta_x A + \eta_y B$ result from the linearization of the flux vectors $\hat{F} = (\xi_x F + \xi_y G) / J$ and $\hat{G} = (\eta_x F + \eta_y G) / J$, respectively; with $A = \partial F / \partial U$ and $B = \partial G / \partial U$.

Furthermore, for steady-state computations:

$$\begin{aligned}\Omega_{i+1/2,j}^{\xi} E^* &= M_{i+1/2,j}^{\xi} I(E_{i+1,j}^* - E_{i,j}^*) \\ \Omega_{i,j+1/2}^{\eta} E^n &= M_{i,j+1/2}^{\eta} I(E_{i,j+1}^n - E_{i,j}^n)\end{aligned}\quad (72)$$

The values $M_{i+1/2,j}^{\xi} = \max[\psi(a'_{i+1/2})]$ and $M_{i,j+1/2}^{\eta} = \max[\psi(a'_{j+1/2})]$ are the maximum scalar values of the entropy correction function ψ defined in Eq. (24). $a'_{i+1/2}$ and $a'_{j+1/2}$ are the eigenvalues corresponding to the Jacobian matrices \hat{A} and \hat{B} , respectively. The quantities with the superscript l present arrays with 4 elements, $l=1,2,3,4$. The RHS here is a combination of a cell-vertex finite-volume approach and the numerical dissipation of the Yee's TVD scheme as^[20]:

$$\begin{aligned}RHS &= \frac{-\Delta t_{i,j}}{A_{i,j}} \sum_{AB}^{DA} (F \Delta y - G \Delta x) \\ &\quad - \frac{\Delta t_{i,j}}{2} \left[(R_{i+1/2,j} \Phi_{i+1/2,j} - R_{i-1/2,j} \Phi_{i-1/2,j}) + (R_{i,j+1/2} \Phi_{i,j+1/2} - R_{i,j-1/2} \Phi_{i,j-1/2}) \right]\end{aligned}\quad (73)$$

The elements of array $\Phi_{i+1/2}$ denoted by $(\phi'_{i+1/2})^U$ for the second-order upwind TVD scheme are given by^[20]:

$$(\phi'_{i+1/2})^U = \frac{1}{2} \psi(a'_{i+1/2}) (g'_{i+1} + g'_i) - \psi(a'_{i+1/2} + \gamma'_{i+1/2}) \alpha'_{i+1/2}\quad (74)$$

With the functions and defined as:

$$\gamma'_{i+1/2} = \frac{1}{2} \psi(a'_{i+1/2}) \begin{cases} (g'_{i+1} - g'_i) / \alpha'_{i+1/2} & \alpha'_{i+1/2} \neq 0 \\ 0 & \alpha'_{i+1/2} = 0 \end{cases}\quad (75)$$

and

$$\psi(z) = \begin{cases} |z| & |z| \geq \varepsilon \\ (z^2 + \varepsilon^2) / 2\varepsilon & |z| < \varepsilon \end{cases}\quad (76)$$

With $\varepsilon = 0.125$. The characteristic function $\alpha'_{i+1/2}$ is defined as:

$$\alpha'_{i+1/2} = R_{i+1/2}^{-1} (U_{i+1} - U_i)\quad (77)$$

Where \underline{g} is the right eigen-vector matrix. Here, the Van-Leer limiter function $g_{i+1/2}^l$ is used as

$$g_i^l = \frac{\left\{ \alpha_{i-1/2}^l \left[(\alpha_{i+1/2}^l)^2 + \delta \right] + \alpha_{i+1/2}^l \left[(\alpha_{i-1/2}^l)^2 + \delta \right] \right\}}{\left[(\alpha_{i+1/2}^l)^2 + (\alpha_{i-1/2}^l)^2 + 2\delta \right]} \quad (78)$$

With δ as a small parameter ($10^{-7} \leq \delta \leq 10^{-5}$). ~~Roe's averaging is used to evaluate $U_{i+1/2}$ and the corresponding terms~~^[20].

5.3. Baldwin-Lomax Turbulence Modeling

In the Baldwin-Lomax two layer formulations, the coefficient of turbulent viscosity is given by^[20]:

$$\mu_t = \begin{cases} (\mu_t)_{inner}, & y \leq y_c \\ (\mu_t)_{outer}, & y > y_c \end{cases} \quad (79)$$

Where y is the local distance measured normal to the body surface and y_c is the smallest value of y at which the values from the inner and outer region formulas are equal. In practice y_c corresponds to the y at which

$(\mu_t)_{inner} \geq (\mu_t)_{outer}$. Within the inner region,

$$(\mu_t)_{inner} = \text{Re}_\infty \rho l_m^2(y) |\omega| \quad (80)$$

Where ω is the vorticity defined by

$$\omega = \frac{\partial u}{\partial y} - \frac{\partial v}{\partial x} \quad (81)$$

And l_m is the mixing length defined by^[20]

$$l_m(y) = Ky \left[1 - \exp(-y^+ / A^+) \right] \quad (82)$$

where $y^+ = \text{Re}_\infty \frac{\sqrt{\rho_w \tau_w}}{\mu_w} y$ is the non-dimensional distance from wall and

$\tau_w = \frac{\mu_w}{\text{Re}_\infty} \left(\frac{\partial u}{\partial y} \right)_w$ is the wall shear stress.

The outer region formulation is given by^[20]

$$(\mu_t)_{outer} = \text{Re}_\infty C_{cs} C_{cp} \rho F_{wake} / F_{kleb} \quad (83)$$

where F_{wake} is the maximum value of the function

$$F(y) = \frac{l_m(y) |\omega|}{K} \quad (84)$$

and F_{kleb} is the Klebanoff intermittency factor defined as

$$F_{kleb} = \left[1 + 5.5 \left(\frac{C_{kleb} y}{y_{max}} \right)^6 \right] \quad (85)$$

y_{max} being the value of y for F_{max} . To determine each peak in F , it is suggested that the value $F_{peak} = F(y_{peak})$ is chosen when $F(y) < 0.9 F(y_{peak})$ for $y > y_{peak}$ ^[20].

The turbulence model involves with the following five constants:

$$K = 0.41, A^+ = 26, C_{cs} = 0.0168, C_{cp} = 1.6, \text{ and } C_{kleb} = 0.3.$$

Since the zero-equation turbulence model cannot predict the transition from laminar to turbulent, the transition position was fixed at three percent (%3) of the aerofoil leading edge for all computations.

5.4. Lift and Drag of Circulating NACA0015 Aerofoil

For computation of 2D compressible flows over the symmetrical NACA0015 aerofoil, the C-type algebraic-hyperbolic mesh of 141×101 was constructed. As shown in Fig. 20. The aerofoil is placed at a distance nearly equals to thirteen times the chord length from the leading and trailing edges and far filed boundary was stretched to nineteen times the chord length as shown in Fig. 20. The stretching of mesh in the boundary layer is controlled by the distance of the first mesh point from the surface such that 15 to 20 mesh points are placed in the boundary layer. As the initial condition ($t=0$), all the quantities was set to their free stream values, which means that the aerofoil is inserted suddenly into an undisturbed flow with free stream condition specified everywhere. The free stream Mach number was set to $M_\infty = 0.2$ for producing comparable results with incompressible flow solutions

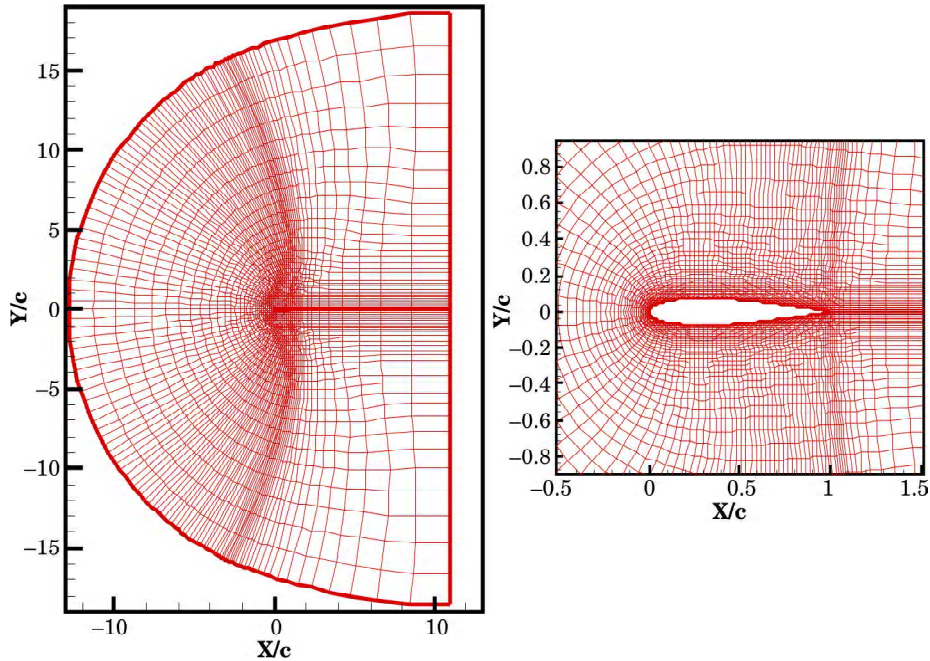


Fig. 20: The C-type 141×101 mesh of algebraic-hyperbolic around NACA0015 aerofoil

and the Reynolds number was specified as $Re = 3.6 \times 10^5$. The transition position has very important rule in the zero equation such as Baldwin-Lomax turbulence model to accurately predict correct solutions even for attached flows. The choice of transition position here should be accompanied with some stability codes to accurately predict its position. However in this study, the transition position was fixed at three percent (%3) of the chord length for all computations to just see the overall trends of the circulating aerofoil.

In Fig. 21, the trends of lift coefficient are shown for NACA0015 at different circulating speeds of 0, 0.2, 0.5, 1, 2, and 3 versus incidence angles and also compared with the widely cited experimental results of^[21]. As seen in Fig. 21, the present computations are merely close to experiments in low incidence angles in the linear region; however, the results mismatch considerably at higher incidence angles when separation zones develop and stall occurs. The present computational results can be improved by assigning the correct transition position which can be obtained from some stability codes. But, more advanced turbulence models should be implemented and more wind tunnel testing should be carried out to validate such modelling for circulating aerofoils. Thus, the following solutions are not seen as correct solutions except it just shows the merits of the aerofoil-Magnus blades and also gives some guidelines for further research.

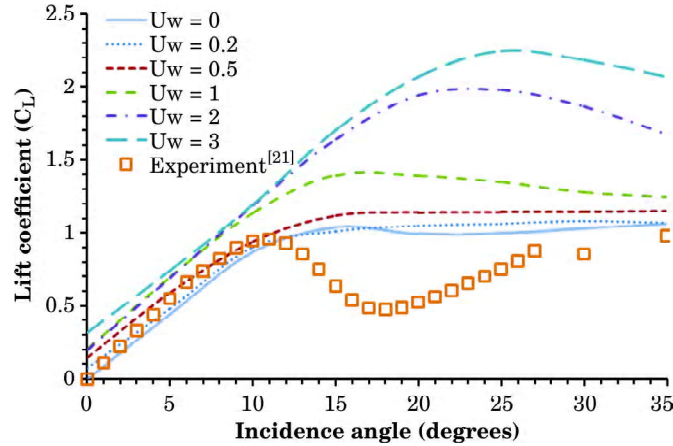


Fig. 21: Lift coefficient of NACA0015 aerofoil at different treadmill speed ratios versus incidence angle ($M_\infty = 0.2$, $Re_\infty = 3.6 \times 10^5$).

From the experiments, it is evident that the fixed aerofoil stalls at incidence angles of 15 degrees and higher. For the circulating aerofoil as expected, the stall angle and also lift coefficient are increased by increasing treadmill speed of the circulating aerofoil. At the treadmill speed ratio of 3, the stall angle is increased to 25 degrees and the lift coefficient is also doubled.

Figure 22 shows the drag coefficient at different treadmill speeds versus incidence angle. In comparison with experiment, the present computation over predicts the drag force in low angles of attack and under predicts the drag at high incidence angles. However, it is interestingly seen that the drag coefficient is favourably decreased by increasing the treadmill speed.

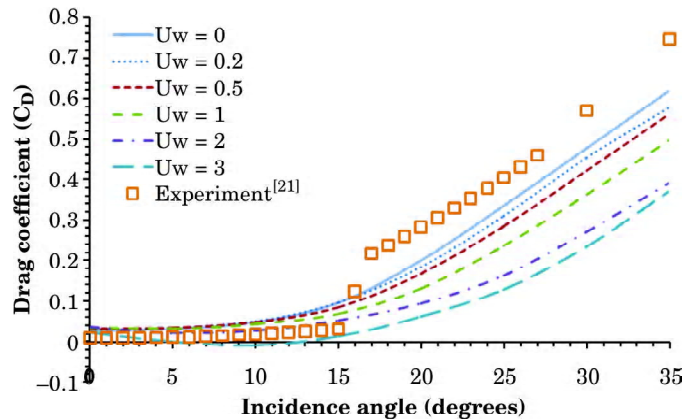


Fig. 22: Drag coefficient of NACA0015 aerofoil at different treadmill speed ratios versus incidence angle ($M_\infty = 0.2$, $Re_\infty = 3.6 \times 10^5$).

The minimum drag occurs at the treadmill speed ratio of 3 and incidence angles within the range of 5 to 15 degrees. In this treadmill speed ratio of 3, the drag coefficient reduces to its minimum and change sign to negative values.

Figure 23 shows a decreasing trend for the distribution of drag to lift ratio at different treadmill speed ratios versus incidence angles. Again, the difference between computation and experiments is considerable. At the treadmill speed ratio of 3, the lowest drag to lift ratios is obtained in the same range of incidence angles between 5 to 15 degrees. For instance at the incidence angle of 5 degrees and treadmill speed ratio of 3, the lift to drag ratio can attain a remarkably high value of 684 which is three times higher than the best wind turbine aerofoils in operation. This can be great achievement for such simple aerofoil geometry; because, the non-circulating NACA0015 aerofoil posses the maximum lift to drag ratio of nearly 50 at incident angle of 10 degrees.

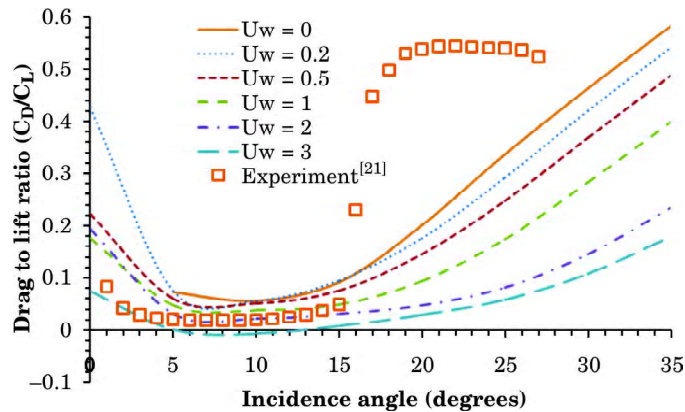


Fig. 23: Drag to lift ratio of NACA0015 aerofoil at different treadmill speed ratios versus incidence angle ($M_\infty = 0.2$, $Re_\infty = 3.6 \times 10^5$).

5.5. Field Contours Around Circulating NACA0015 Aerofoil

Figures 24 to 26 show the streamlines and pressure contours at the incidence angles of 0, 5, and 10 degrees; respectively, at the desirable treadmill speed of 3.

From the streamlines shown in Figs. 24 to 26, it is evident that the separation zone underneath the aerofoil surface is progressively reduces size by increasing the aerofoil incidence angle.

At low treadmill speed of 1.0 and high incidence angles of 15, 25, and 35, the results for streamlines and Mach contours are shown in Figs. 27, 28, and 29; respectively. From these figures, it is evident that a separation

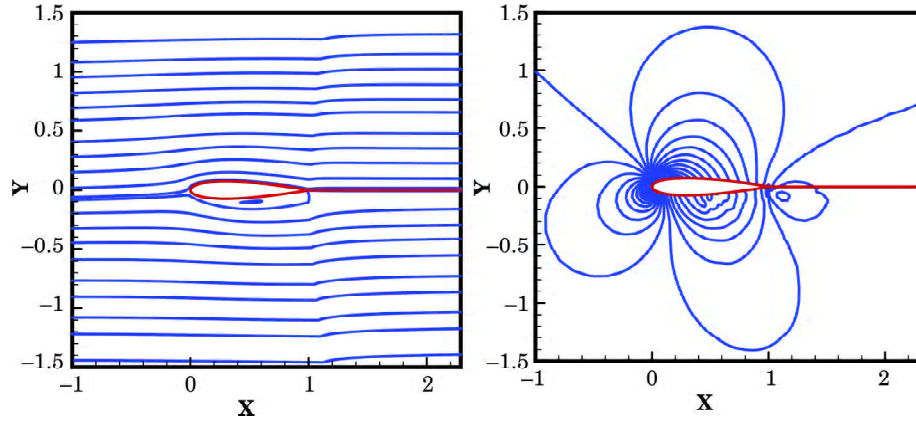


Fig. 24: Streamlines and pressure contours over NACA0015 aerofoil at zero angle of attack and the treadmill speed of 3.0 ($M_\infty = 0.2$, $Re_\infty = 3.6 \times 10^5$).

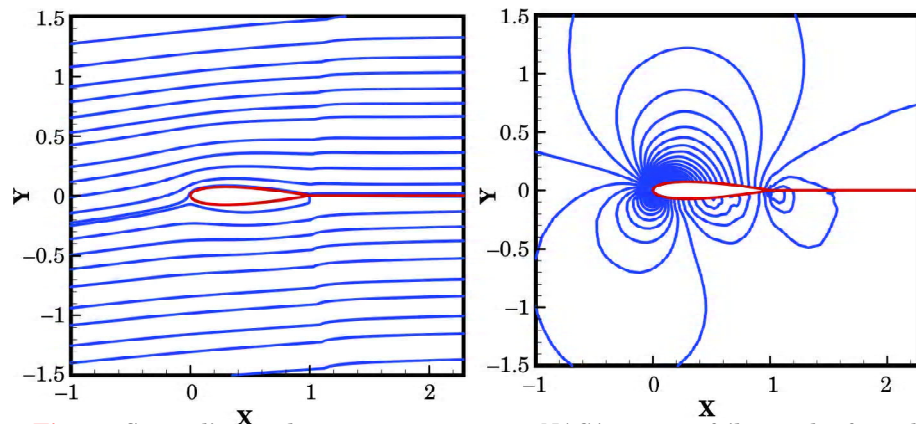


Fig. 25: Streamlines and pressure contours over NACA0015 aerofoil at angle of attack of 5 degrees and the treadmill speed of 3.0 ($M_\infty = 0.2$, $Re_\infty = 3.6 \times 10^5$).

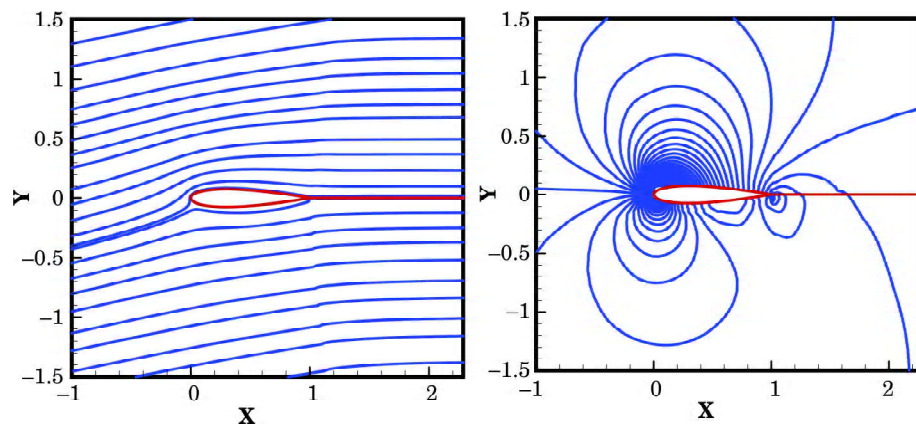


Fig. 26: Streamlines and pressure contours over NACA0015 aerofoil at angle of attack of 10 degrees and the treadmill speed of 3.0 ($M_\infty = 0.2$, $Re_\infty = 3.6 \times 10^5$).

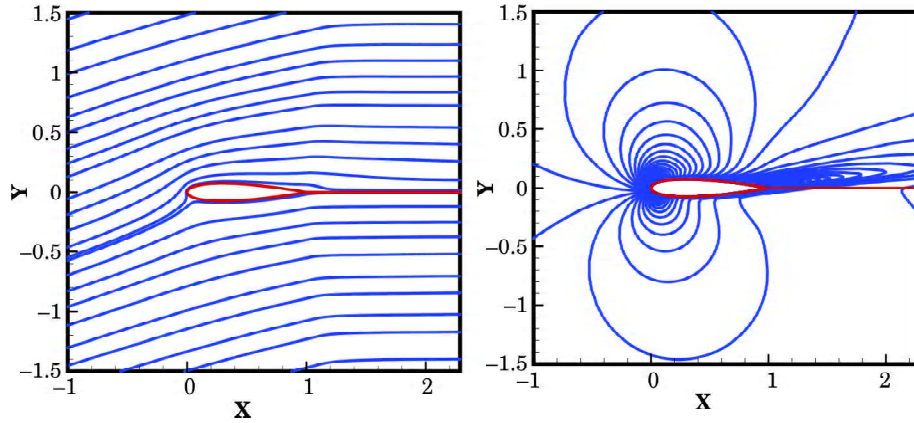


Fig. 27: Streamlines and contours of Mach number over NACA0015 aerofoil at constant treadmill speed of 1.0 with the angle of attack of 15 degrees ($M_\infty = 0.2$, $Re_\infty = 3.6 \times 10^5$).

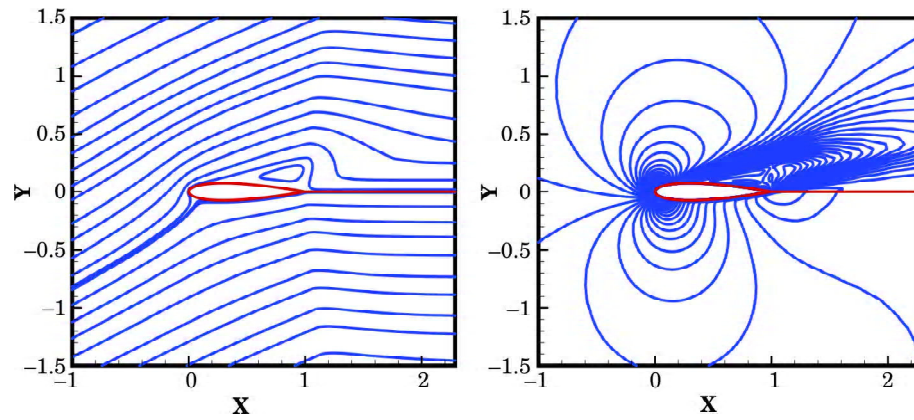


Fig. 28: Streamlines and Mach no. contours over NACA0015 aerofoil at constant treadmill speed of 1.0 with the angle of attack of 25 degrees ($M_\infty = 0.2$, $Re_\infty = 3.6 \times 10^5$).

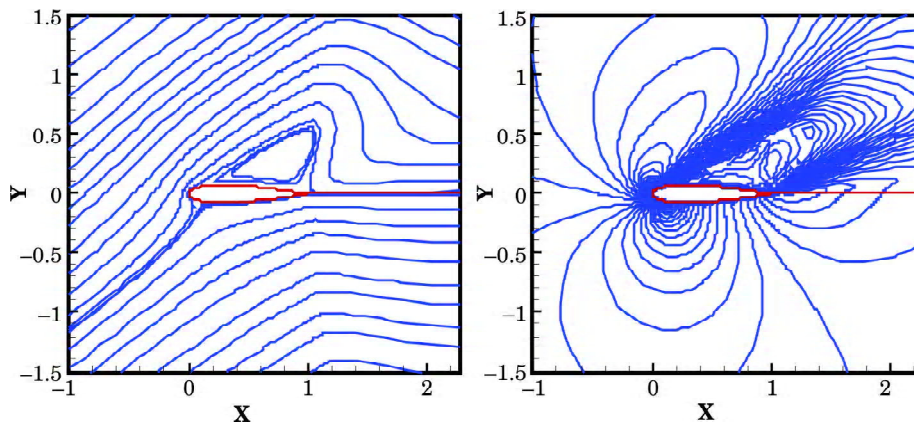


Fig. 29: Streamlines and Mach no. contours over NACA0015 aerofoil at constant treadmill speed of 1.0 with the angle of attack of 35 degrees ($M_\infty = 0.2$, $Re_\infty = 3.6 \times 10^5$).

zone is progressively grows on the upper aerofoil surface. This separation zone is the major cause on reducing rate of increase of lift and increase of drag at high incidence angles.

From this study, it is realized that many aerofoil geometries, with ease of manufacturing, can be feasibly studied to implement the treadmill motion. Some experimental studies may be conducted to find an optimum blade section for operation in aerofoil-Magnus type wind turbines. Such progress studies as outlined in this paper allows development of innovative wind turbines by saving efforts and costs towards more efficient and less expensive wind turbine systems.

6. CONCLUSIONS

The subject of using Magnus force from rotating bodies is reviewed for application in innovative wind turbines. It is appeared that there is a growing interest in Flettner type ships in naval engineering due to increasing trends of fossil fuel costs and climate change concerns. There is also some progress in development of Magnus type horizontal axis wind turbines which will benefit to other fields in naval or aerospace engineering. The subject of Magnus effects were extensively reviewed by Seifert in aerospace engineering who highlighted the lack of specific methods and modelling on design of lifting devices from the Magnus effects. This paper is particularly focused on development and extension of models and theories that are usually used in wind energy community to model and to extend our understanding from the horizontal axis Magnus type wind turbines. It is well known that the drag to lift ratio is the most crucial parameter in designing and modelling the aerofoil type commercial type wind turbines; likewise, the findings of this work suggests that the success of any Magnus type wind turbine may be strongly dependent on reducing the drag to lift ratio. The BEM results on power coefficient of Magnus type wind turbine using cylindrical rotors may show some merit for some small applications; however, more experimental works on innovative application of Magnus effect is still needed to guarantee success of using Magnus force in large scale wind turbine applications. From the experimental results on drag and lift of spinning cylinders, the optimum value of drag to lift ratio is suggested equals to 0.2 which only produces the power coefficient of 0.35 at the blade speed ratio of unity. This is not as yet promising for small wind turbine applications in low wind speeds; unless such designs as Murakami's Magnus wind turbine with spiral ribs have improved such poor performance. In general however, the power capture from rotating blades of Savonius or cylindrical sections is very low due to very high drag to lift ratios. Therefore, the emerging aerofoil Magnus type wind turbine concept may overcome this by utilizing the treadmill motion of aerofoil surfaces. Simple and easy to manufacture aerofoils may then be used. In this work, the computation of viscous flows around circulating NACA0015 aerofoil revealed that the

circulating aerofoils may considerably increase the lift to drag ratio by several times than the conventional aerofoils. For instance, the maximum lift to drag ratio of 684 is achieved by the symmetrical NACA0015 aerofoil at the circulating speed ratio of 3 and incidence angle of 5 degrees. The present computational results on the emerging aerofoil-Magnus type wind turbines needs further improvements by employing more advanced turbulence models and with validating present results using wind tunnel measurements. The prospectus of using such new generators is fascinating and absolutely promising.

REFERENCES

- Seifert, J. 2012. A review of the Magnus effect in aeronautics. *Prog. Aerosp. Sci.*, 55: 17–45.
- Bychkov, N.M., Dovgal, A.V. and Kozlov, V.V. 2007. Magnus wind turbines as an alternative to the blade ones. *J. Phys. Conf. Series*, 75: 012004.
- Murakami, N., Akita, J.P., Ito, J. and Akita, J.P. 2007. Magnus type wind power generator. US Patent, 0046029: A1.
- Murakami, N. and Akita, J.P. 2010. Magnus type wind power generator. US Patent, 0038915: A1.
- Mecaro Co. Japan. 2013. <www.mecaro.jp/eng/> [accessed 11.01.13].
- Giudice, F. and La Rosa, G. 2009. Design, prototyping and experimental testing of a chiral blade system for hydroelectric microgeneration. *Mech. Mach. Theo.*, 44: 1463–1484.
- Komatinovic, N. 2006. Investigation of the savonius-type magnus wind turbine, MSc thesis, MEK, Technical University of Denmark.
- Reid, E.G. 1925. Tests of rotating cylinders. *Flight*.
- Glauert, M.B. 1957. A boundary layer theorem, with applications to rotating cylinders. *J. Fluid Mech.*, 2: 89.
- Ingham, D.B. 1983. Steady flow past a rotating cylinder. *Comput. Fluids*, 11(4): 351–366.
- Mittal, S. and Kumar, B. 2003. Flow past a rotating cylinder. *J. Fluid Mech.*, 476: 303–334.
- Tokumaru, P. and Dimotakis, P. 1991. Rotary oscillation control of a cylinder wake. *J. Fluid Mech.*, 224: 77–90.
- Badalamenti, C. and Prince, S.A. 2008. The effects of endplates on a rotating cylinder in crossflow, AIAA, 7063.
- Thouault, N., Breitsamter, C., Seifert, J., Badalamenti, C., Prince, S.A. and Adams, N.A. 2010. Numerical analysis of a rotating cylinder with spanwise discs, 27th International Congress of the aeronautical Sciences, ICAS.
- Labraga, L., Bourabaa, N. and Berkah, T. 2002. Wall shear stress from a rotating cylinder in cross flow using the electrochemical technique. *Exp. Fluids*, 33: 488–496.
- Munson, B.R., Rothmayer, A.P., Okiishi, T.H. and Huebsch, W.W. 2012. *Fundamentals of fluid mechanics*. Wiley; 7th edition.
- Burton, T., Sharpe, D., Jenkins, N. and Bossanyi, E. 2001. *Wind energy handbook*. John Wiley & Sons, LTD, Chichester.
- Sedaghat, A. A closed form mathematical extension to BEM analysis of horizontal axis wind turbines, (submitted to IEEE).
- Flettner, A. 1923. German Patent, No. 420840.
- Sedaghat, A. 1998. A finite volume TVD approach to transonic flow computations. PhD thesis, The University of Manchester.
- Sheldahl, R.E. and Klimas, P.C. 1981. Aerodynamic characteristics of seven symmetrical airfoil sections through 180-degree angle of attack for use in aerodynamic analysis of vertical axis wind turbines, Sandia National Laboratories, Energy Report SAND80-2114.